Utrecht University

Graduate School of Natural Sciences
MSc in Climate Physics

Characterizing cold pool interactions over land

with observational data from the Netherlands

Irene Livia Kruse

Supervisors:
Aarnout J. Van Delden (IMAU)
Jan O. Haerter (NBI)
Bettina Meyer (NBI)

Utrecht and Copenhagen, August 2020

Abstract

When precipitation evaporates in a sub-saturated boundary layer, it cools the air and produces dense downdrafts, which sink towards the surface and can spread horizontally as a density current. These spreading "cold pools" (CPs) can trigger convection and thus new precipitation events due to dynamical and thermodynamical lifting mechanisms. Due to their role in the organization of convection, CP properties are currently being studied with the use of high-resolution numerical simulations. Measurement campaigns have been conducted over the ocean to validate the models. However, fewer studies have targeted ensembles of cold pools over land. We use the observational network of the Netherlands, specifically the 213m Cabauw boundary layer measurement tower and the Herwijnen polarimetric radar, to study CPs developing from summer convection and their role in triggering new convective events over land. We create an algorithm that detects the passage of a CP from the Cabauw tower time series to automatize the detection of CPs from a point measurement time series. The detected CP gust fronts and their generating precipitation cells are studied with imagery from the Herwijnen radar, situated in proximity to the Cabauw tower. We explore the characteristics of the CP gust fronts and interiors with the Cabauw tower time series, and specifically look for evidence of vortex rings, accumulated moisture in the leading edge and dry interiors. Gathering all the CP cases found, we show the measured CP properties in dependence of the precipitation intensity of the generating precipitation cell, and of the environmental conditions. We find positive correlations between the temperature drops and the wind gusts associated with the CPs, and explore the correlations between these properties, the precipitation intensity of the generating cells, and the mean atmospheric moisture before the event. These links will help gain more insight into the role of CPs in organizing convection over land.

Acknowledgements

This thesis was driven by curiosity, and aided by a vast collection of other curious minds who gave me their insight and time, whether it be in the form of physical meetings, or providing me with observational data. I firstly thank Jan (Haerter), who introduced me to this captivating world of cold pool dynamics and welcomed me into his research group, namely the Atmospheric Complexity group at the Niels Bohr Institute in Copenhagen. Next to Jan, is Bettina (Meyer), who took me under her wing and mentored me throughout my whole project. I am thankful for Aarnout (Van Delden)'s continuous support from the side of my home university (Utrecht University), and the meetings with his Atmospheric Dynamics group at the Institute for Marine and Atmospheric research. Special mention to Michiel (Baatsen) for his broad knowledge about thunderstorms and for helping me find perfect convective summer days. Bram (Van 't Veen) enabled me to observe cold pools in radar data, thanks to his powerful radar data viewer, NLradar, and his helpful advice. I thank Fred (Bosveld) who was always open to helping me find data from the Cabauw tower and finally Louise (Nuijens) and Adrian (Tompkins) who both dedicated time to thought-provoking chats about cold pools.

Contents

Chapter 1

Introduction

Imagine yourself sitting outside on a warm and sunny summer afternoon, and noticing a massive cloud suddenly forming in the distance, as in figure 1.1.

Figure 1.1: A convective cloud developing in the distance on a clear summer afternoon, as seen from Utrecht on August 27, 2019.

The cloud darkens and you can see the rain falling from it as it takes on the likings of a thunderstorm. It slowly moves towards you and before you know it, you feel a gust of cold wind and the temperature has dropped to the point that you need to put on a jumper. With this thesis we aim to investigate the dynamics of exactly that gust of cold air, which originates from the precipitating storm cloud and spreads out in all directions. We identify the mass of cold air of which the boundaries are marked by the spreading gust front, as a "cold pool". We will use observational data to find a way to clearly observe these cold pools, to better understand their dynamics.

The key to understanding the scientific community's renewed interest in cold pools lies within the concept of *convective organization*. First, one has to understand what convection is, and how it leads to the formation of clouds, precipitation, and cold pools. Convection describes the vertical movement of air within the atmosphere, which typically is initiated at a strongly heated surface. A heated surface will heat the overlying air, which expands and becomes less dense than the surrounding air. This allows air to rapidly rise, much like what happens when you heat a pot of water on the stove and bubbles form and rise. The surface can also be a moisture source, which can evaporate and rise along with the rising air. When this water vapour condenses at higher levels, heat is released due to condensation, enhancing the upward convective motion. These

updrafts can then form convective clouds, which can eventually produce very strong and localized precipitation [21]. This precipitation can evaporate when falling, cooling the air and thereby creating a downdraft of cold air, which spreads out when hitting the surface, giving birth to the aforementioned cold pool. The link between this smaller-scale phenomenon (on the order of 1-10 km horizontally) to the large-scale spatial organization of the cloud field in the order of 100+ km - *convective organization* - is explored in both theoretical studies (e.g. [35] [15] [13] [12]) and observational studies (e.g. [38] [10] [40]).

A cold pool can interact dynamically and thermodynamically with its environment, producing new updrafts and potentially new convective clouds, that in turn can result in a new precipitation event, which produces a new cold pool and so on. The cold pools are therefore a way for convective clouds to interact with their surroundings and with each other, and may be a key ingredient to understanding how clouds organize spatially and temporally into larger-scale precipitating systems. An observable example of an organized convective system is an MCS (mesoscale convective system), a complex of thunderstorms which spans more than 100 km in diameter, that is generally long-lived and can produce intense precipitation. Understanding how the convective cloud field organizes, accompanies other scientific questions; namely how the organization of the cloud field impacts the precipitation intensity (that affects us humans directly), and how it impacts the radiative feedback of the atmosphere. In both of these cases it becomes important to understand the underlying mechanisms of the organization. If we understand the underlying mechanisms, we can find out how the organization of clouds might be affected by a warming climate, thus affecting the precipitation intensities. If we understand the impacts of cloud organization on the radiative feedbacks, we can furthermore understand how it might contribute to modulating the climate itself. If the organization of convective clouds should in fact change under a warmer climate, this could have implications for the degree of warming. A prominent example of one of the possible kinds of (negative) feedback on rising temperatures due to cloud organization, is the one seen in simulations showing the phenomenon of self-aggregation [36]. In these simulations, the convective cloud field clusters in space over time scales of days-months, and although the mechanisms behind this clustering are not yet fully settled, the phenomenon leads to an effective loss of radiation and thus heat from the atmosphere to space [5].

Since cold pools are a phenomenon nested within the convective cycle, it is necessary to understand their dynamics, to then be able to understand their contribution to the convective cycle and to the organization of convective clouds. On a time scale that is easier to measure with meteorological data, understanding cold pool dynamics can also be interesting for short term forecasting purposes, as the gust fronts produced can be troublesome e.g. for aviation [19]. It can also be useful to understand in which conditions cold pools contribute to forming new precipitation events, to have a better idea of where new thunderstorms might occur most probably in a given area.

The dynamics of cold pools is currently being intensely studied with numerical simulations that are now able to resolve the spatial scales needed to describe these phenomena, i.e. spatial grids of less than 1 km (e.g. [9] [11] [7]). It is useful to have a means of comparison and validation for numerical studies, with the use of observational data. Oceanic measurement campaigns have provided insights into the dynamics of ensembles of cold pools over the tropical and subtropical oceans (e.g. [28] [39] [32] [37]). Some observational studies have targeted cold pools over land, but mostly focusing on single case studies (e.g. [24] [33]).

This thesis thus aims to provide an observational-based analysis of cold pools over land, with a focus on their interactions with the environment. We try to find simplified cold pool cases and collect existing data to study them. We develop a method to detect cold pools from weather tower measurements, and utilize radar imagery to visualize the dynamics of cold pools on the horizontal plane. There is a vast reservoir of unused data for this scope. We use the extensive observational data sets from the Netherlands, combining meteorological tower data (from the 213m weather mast located in Cabauw), and a country-wide network of meterological stations, and Doppler radar data (from the radar tower located in Herwijnen), to study isolated cold pools and their connection with the environment and their generating precipitation events. Using data from the Netherlands has advantages: the measurements are dense in time and space, and the nearly flat topography of the country is ideal for such a study, as it allows to neglect the influence of topographical triggering

of convection.

A novelty of this study is to use radar imagery to not only look at precipitation intensity, but also visually identify the dynamics of cold pools during their lifetime. This makes use of the fact, that under certain conditions it is possible to observe cold pool edges in radar reflectivity images. This is due to the presence of insects and/or dust that are lofted by converging air along the outflow boundaries, to a height where they can be detected by radar (100-1000 meters above the surface) [33] [20]. Which conditions enable the visualization of these so-called "reflectivity fine lines" [22] remains an open question.

In the *Background* section (Chapter 2) of this thesis, a theoretical and literature-based review is presented on what is known about cold pools. In the *Methods* section (Chapter 3), the data and algorithm used to observe and detect cold pools are presented. In the *Results* section (Chapter 4) we present the findings of the study. Two case studies are examined, exploring the observational data sets. The first event consists of an isolated event which occurred over the Herwijnen tower on August 27, 2019. The second consists of three colliding cold pool gust fronts which occurred over Herwijnen tower on May 29, 2018. Based on these case studies, an algorithm is developed, to identify the passage of cold pools from the local time series measurements of Cabauw tower. This algorithm allows us to identify 18 cold pool events in the period May - September 2019, and 286 cold pool events in the 15 year period 2005 - 2019. This allows us to investigate the changes in the meteorological state before, during and after the passing of the cold pool front. We try to find evidence of moisture rings in the moisture measurements [29] [18] and vortex rings in the imprint of vertical velocity measurements [25], as numerical and theoretical studies find in the cold pool head. The radar imagery corresponding to the identified cold pools is studied. We specifically look for links between the properties of the cold pools themselves, the environmental conditions and the precipitation intensity of cold pool generating events.

Chapter 2

Background

2.1 Convection and Cold Pools

Convection is a natural phenomenon that occurs in the atmosphere and denotes the vertical displacements of air due to density (or temperature) gradients. This vertical motion can be initiated in various ways. *Free convection* refers to the rising of heated surface air, which acquires positive buoyancy by being less dense than its environment, and the sinking of cooler air aloft, which can acquire negative buoyancy by being more dense than its environment. *Forced convection* refers to the lifting of air along a front or a topographic barrier [4].

As moist air rises in the atmosphere, it cools. This is due to the fact that an air parcel undergoes an approximately adiabatic expansion as it rises to higher altitudes and thus lower air pressures. At a certain altitude (namely, the *lifting condensation level*), the temperature of the rising air parcel reaches its dew point and becomes saturated. At this point, condensation begins and a cloud starts forming. In figure 2.1a the birth of a convective cloud is visualized. The cloud continues to grow in a conditionally unstable atmosphere (i.e. when the environmental temperature profile is such that the saturated rising air parcel is constantly warmer than the air surrounding it) as long as it is fed by rising air from below. Water vapor in the rising air condenses into liquid or solid cloud particles thereby releasing latent heat, which keeps the air warm and positively buoyant. When the cloud particles reach the freezing level, they grow larger and become heavier, and eventually begin to fall as precipitation. Drier air surrounding the cloud is also drawn into the cloud (phenomenon known as *entrainment*), and can descend as a convective downdraft. This phenomenon effectively dilutes the cloud, as while dry air enters the cloud, moist air must leave the cloud. In figure 2.1b, a mature, precipitating convective cloud is schematized along with convective updrafts (red arrows), entrainment (blue arrows entering the cloud from the upper atmosphere) and downdrafts (blue arrows) [4].

Within the field of atmospheric convection, the term "cold pool" indicates a region of cold air produced by the partial evaporation of precipitation falling from a (convective) cloud into a subsaturated atmosphere. The cold air produced this way descends partly due to its negative buoyancy and partly due to the drag exerted by the falling rain drops. When it hits the ground, it spreads out horizontally, away from the source, introducing cold dense air underneath warmer environmental air, and thus moving as a density current [8]. The outer edge of the spreading cold pool often is referred to as the "outflow boundary", or the "gust front". In figure 2.1b we can see the cold pool spreading underneath the cumulonimbus cloud and in figure 2.1c we see a schematic of the final stage of dissipation of the convective event. Outflows are generally on the order of 1 km deep, with the depth depending on how long the parent convective cell has persisted [21]. The temperature deficit within a cold pool depends on the environmental atmospheric profiles of temperature and relative humidity. The coldest outflows will stem, for example, from high-based thunderstorms that rain into very dry boundary layers [21].

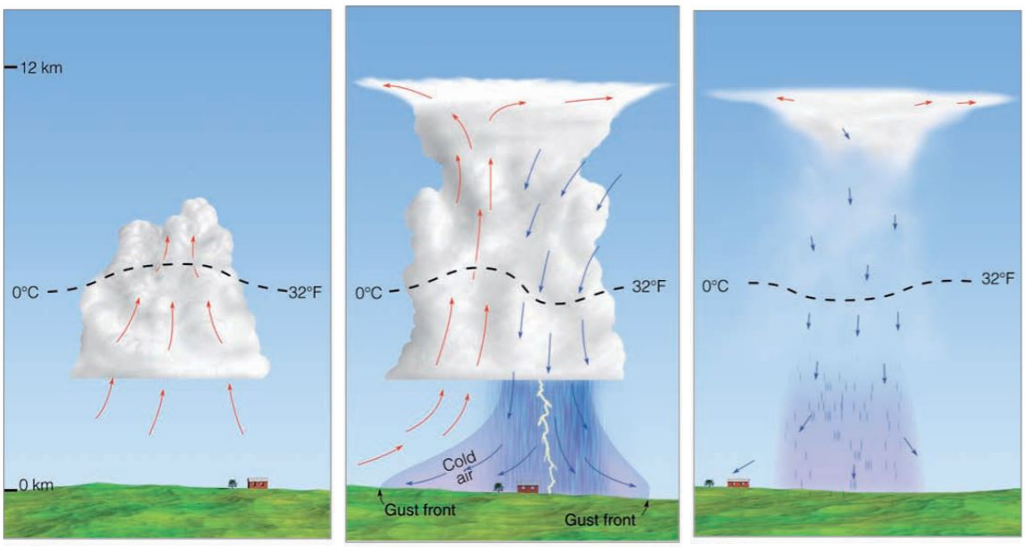

(a) (b) (c)

Figure 2.1: Schematic of the development of a deep convective cloud (a), cold pool formation (b) and successive dissipation (c). [21]

2.2 Laboratory Studies

Some cold pool properties can be approximated and studied in laboratory settings with the theory of density currents. A density current is the flow of dense fluid within a lighter fluid. A cold pool spreading in the atmosphere is a good example of a density current as it consists of dense, cold outflow air moving through the less dense environmental air. The driver of density current motion is the horizontal pressure gradient force present across the density interface due to the density difference [22]. This density interface behaves in general as a material surface, not allowing air parcels to pass through but rather pushing them over the travelling denser air. Density currents have a leading edge (also called head) which is typically deeper than the fluid behind the leading edge. Many laboratory studies have tried to reconstruct density currents to study their properties (e.g. [27] [23] [16]). In figure 2.2, we see a snapshot of a density current created in a laboratory tank [27]. The density current in this study is created by letting a denser liquid flow freely through a long, narrow tank filled with a less dense liquid. In the figure, it is passing the 100 cm mark from a lock extending from 0 to 20 cm, filled to a quarter of its depth with dense fluid. The leading head is visibly deeper than the following flow.

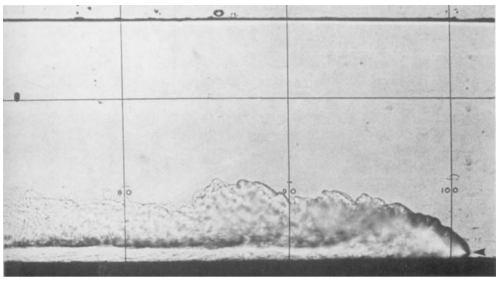

Figure 2.2: Snapshot of density current head, created in a laboratory tank. [27]

In the atmosphere, the depth of the head depends on the magnitude of convergence of air, which in turn depends on the density difference and the environmental wind shear [22]. The spreading velocity of an idealized density current cold pool can be derived as a function of the

density difference (which can be approximated by the difference in temperature) between the colder air and the environmental air, and the depth of the cold pool. The propagation speed c of the gust front can thus be estimated from

$$c \approx \sqrt{gH\frac{\Delta T}{T_0}} \tag{2.1}$$

[26] [22], where g is the gravitational acceleration, H is the height of the density current, ΔT is the temperature difference between the cold pool and the ambient air, and T_0 is the absolute ambient temperature in Kelvin. This does not account for environmental wind shear and surface friction, both of which are present in the real atmosphere. Numerical simulations including wind shear show that when it is present and it points in the direction of the density current motion, density current is slowed relative to the environmental air. In these conditions it also develops a deeper head and more intense lifting at the leading edge [22].

2.3 Cold Pools and Convective Triggering

The properties of cold pools and their role in triggering new convection is currently being studied using numerical simulations and observational data. There is still a need of understanding the processes that determine the evolution in time of cold pool properties, for example their size, strength and lifetime [9]. The paper identifies four stages of a cold pool, as depicted in figure 2.3.

One of the first studies of thunderstorm outflows over land with the use of radar imagery is a paper by R. M. Wakimoto [33], which presents three cold pool cases originating from intensely precipitating organized systems. Each stage of the lifecycle of a cold pool has different measured

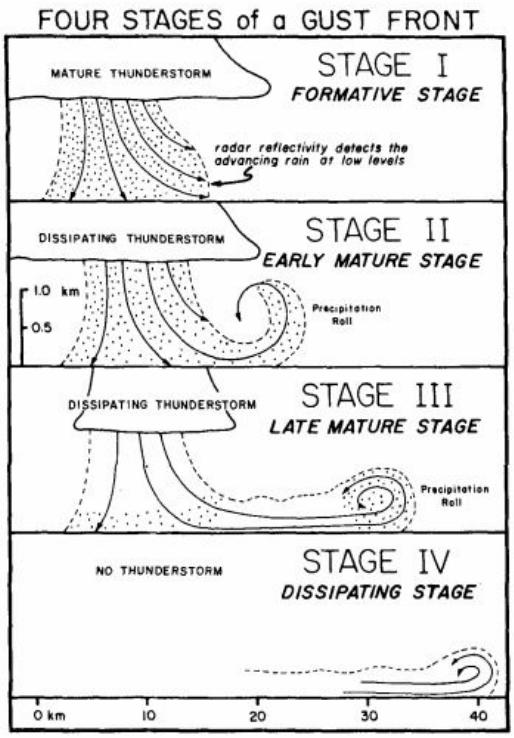

Figure 2.3: Four stages of a thunderstorm gust from, as defined by R. M. Wakimoto. [33].

properties, especially regarding propagation velocity (ranging from 10-30 m/s in the first three stages, and then 5-15 m/s in the last stage) and depth of the head (ranging from larger than 1

km in the first stage to less than 500m in the latest stage). Figure 2.3 shows a schematic of a propagating cold pool [33]. The fact that the cold pool properties change during the lifetime is important to keep in mind when comparing multiple gust fronts measured at a meteorological tower (as we will do), because each case will be at a different stage when passing by the tower. The outer "roll" drawn in the figure along with the leading edge shows up in LES simulations of isolated cold pools. A clear example of this roll is shown in figure 2.4 from a recent study [14]. This so-called *vortex ring* shows up in the outer edge of the cold pool as a peak in horizontal velocity and a dipole in vertical velocity [14] (which we will look for in our observational data). The strength

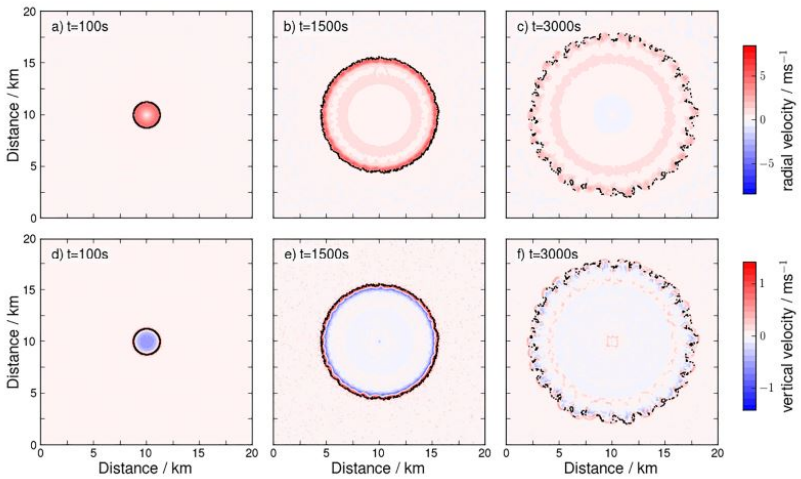

Figure 2.4: Time evolution of an LES-simulated isolated cold pool in terms of the radial velocity (top: a–c) and vertical velocity (bottom: d–f) at the lowest model level at different times [14].

of these updrafts at the leading edge are important (and we wish to quantify them) because they can contribute to the triggering of new convection, if they can lift the air parcels high enough that they become positively buoyant. This mechanism is an example of dynamic convective triggering [30]. Rings of clouds can often be seen in satellite imagery, denoting the outer rim of cold pools. A remarkable example of a ring of clouds developed around a cold pool can be seen in figure 2.5 [40]. Cold pools can collide with other cold pools, displacing vertically the air caught in the points

Figure 2.5: Aircraft view of a cold pool with ring of clouds. [40]

of convergence. This is another dynamic triggering mechanism. Deep clouds tend to form more often at the intersection of multiple cold pools than on the edges of isolated cold pools [10], which could be explained by the fact that the surrounding clouds reduce the entrainment of dry air [6]. Looking at the moisture field, the outer edge of cold pools is generally more moist (thus less dense) than the rest of the environment, according to various simulation studies of deep tropical

convection (as in [29]). The rings of enhanced water vapor content and thus high moist static energy within their leading edges (*moisture rings*) would hypothetically lose their temperature deficit due to surface heat fluxes, becoming positively buoyant and resulting in a possible uplifting of air on the boundaries of mature cold pools [29]. This is referred to as the thermodynamic convective triggering mechanism. We wish to investigate this mechanism by looking for moisture rings in cold pools over land.

The exact convective triggering mechanism of cold pools is still in debate, and is probably a combination of the mechanisms mentioned and depending on the conditions at the boundary and in the environment. A recent study furthermore claims that the properties and impacts of the simulated convective clouds and cold pools compared to those in nature are unclear [10], due to the difficulty in observing cold pools and their interactions. It is however generally accepted that cold pools are triggers for new clouds and precipitation, and therefore a key component in spatially organizing the convective cloud field [30]. This drives the search for better understanding of cold pool properties, which we aim to do in this study with observations over land.

Chapter 3

Methods

3.1 Observational Network Used for this Study

We use observational data from the Netherlands, a low-lying country coasting the Atlantic ocean in the mid-latitudes. There are two main facilities used in this study: the Doppler radar tower located in Herwijnen (51.837 N, 5.138 E) and the 213m boundary layer measurement tower at the CESAR observatory located in Cabauw (51.971 N, 4.927 E). The two stations, together with the full KNMI (the Royal Netherlands Meteorological Institute) weather network are highlighted in figure 3.1. The Herwijnen radar tower and the Cabauw tower are approximately 21 km from each other. The Herwijnen radar tower primarily enables us to study precipitation events that form cold pools, and the Cabauw tower enables us to obtain high temporal resolution measurements during the passage of gust fronts of the evaporatively generated cold pools.

Figure 3.1: A map of the Netherlands and its official weather stations. The locations of the stations used in this study are marked by black rectangles.

Herwijnen radar To study precipitation events we use 5-min time resolution radar imagery from the Herwijnen C-band polarimetric Doppler radar tower. The 5-min temporal resolution volumetric radar data was retrieved from the KNMI Data Portal [2]. The visualization of the volumetric radar data was highly facilitated by the NLradar tool [31] developed by Bram van 't Veen.

A weather radar works by transmitting microwaves that interact with hydrometeors as the waves propagate through the atmosphere. When the radar beam intercepts a "target", some of the energy is backscattered to the radar's receiver. The amount of energy backscattered is converted into the *logarithmic reflectivity factor*, or briefly the *reflectivity*, measured in dBZ. High reflectivity in general implies heavy precipitation. The reflectivity value Z of a volume can be converted into an approximate precipitation intensity R through a Z-R relation such as the Marshall-Palmer relation, $Z = 200R^{1.6}$ [20], assuming a specific drop size distribution. The time it takes for the pulse to complete the trip from the radar to the target and back gives the position in space of the "target". Furthermore, the phase of the backscattered signal, when compared to the returned phase of the previous pulse, gives the (Doppler) radial velocity of the "target", towards or away from the radar tower [20]. The Herwijnen radar scans the surrounding atmosphere at 15 different elevation angles, starting from the horizontal. In figure 3.2 we see a sketch of a weather radar detecting a rain event at different angles.

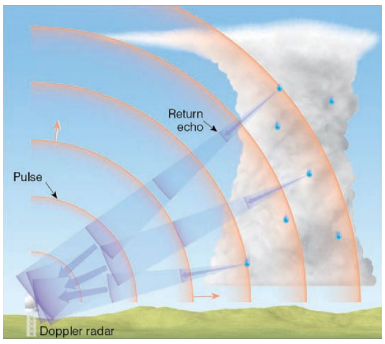

Figure 3.2: Sketch of a weather radar. [4]

The finest radial spatial resolution of the Herwijnen radar is about 225 m and the azimuthal resolution is about 1°. The radar imagery allows us to visualize the properties of the precipitation field associated with cold pool events and at times the cold pool gust fronts. From visual inspection of summer convective precipitation events we noticed that the gust fronts of cold pools at times become visible when the gust front is close to the radar tower. The fact that gust fronts can be visualized in radar reflectivity imagery (as *reflectivity fine-lines*) is not new to the meteorological community [20] and it is a useful tool to dynamically follow the evolution of cold pools. The plausible reason behind the radar-visible gust fronts is that the converging air at the edges of the cold pool may carry insects and dust aloft, which then are intercepted by the radar beam. The radar beam eventually overshoots the height at which these particles are carried, therefore the gust front is only visible when the cold pool is generated close enough to the radar tower. Furthermore, the radar signal weakens away from the tower, leading to a decrease in signal-to-noise ratio.

The use of volumetric radar imagery in this study provides a way to visually confirm the presence of a cold pool by connecting each cold pool signal from the Cabauw tower to a specific generating rain event seen simultaneously by the Herwijnen tower. In some cases the radar imagery allows to follow the dynamical development of the cold pool and successive interactions with its surroundings.

Cabauw tower To study the evolution in time of boundary layer properties before, during and after the passage of a cold pool gust front, we use three observational data sets obtained from the Cesar observatory at Cabauw.

The first data set consists of 10-min point measurements of temperature, horizontal wind speed, wind direction, specific humidity, relative humidity and surface measured rain, measured at the surface and at six different levels of the tower (10m, 20m, 40m, 80m, 140m, 200m), which we use to examine two specific cold pool case studies. The wind speed in this data set is measured with vane anemometers, which enables us only to examine the horizontal component of the wind. This dataset is available online [1].

The second data set consists of 1-min averaged measurements of temperature, dew point temperature, horizontal wind speed, and wind direction at six different levels of the tower (10m, 20m, 40m, 80m, 140m, 200m) for the summer of 2019, and then extended to the years 2005-2019. The wind speed in this data set is measured with the same vane anemometers as in the first, which enables us only to examine the horizontal component of the wind.

The third data set consists of 0.1-sec measurements of water vapor concentration and three-dimensional wind speed measured at three different levels of the tower (60m, 100m, 180m) for the summer of 2019. We take 1-min averages of these time series. The wind speed in this dataset is measured with sonic anemometers, which enables us to examine specifically the vertical wind component. We use this data set to obtain extra information on the cases of the summer of 2019. The second and third datasets were provided by the Cesar observatory upon request [1].

The Cabauw tower is shown in figure 3.3.

Figure 3.3: The 213m boundary layer measurement tower located in Cabauw.

The tower measurements allow us to obtain vertical profiles of the lower atmosphere at any given point in time. This gives valuable information in the event of a passing cold pool, enabling us to understand what the properties of the cold pool front and the cold pool interior are.

WOW-NL We also explore the use of a spatially dense amateur network of meteorological measurement masts (WOW-NL) distributed throughout the country [3]. The temperature data sets are available at a 10-min time resolution, which is lower than the ideal temporal resolution needed to capture spreading cold pool gust fronts in space. However, we can utilize the data set to confirm the cooling at surface level in space, in the presence of a cold pool detected by the point measurements at Cabauw tower.

3.2 Algorithm for Cold Pool Detection

In this section we describe the algorithm created to automatically detect cold pools in the Cabauw tower time series. We base our algorithm on a temperature detection algorithm used in a previous oceanic cold pool study (de Szoeke et al. 2017 [28]), with the addition of wind criteria. We divide the explanation of the algorithm into two parts: temperature criteria and wind criteria.

For any given day, we use the 1-min time series of temperature at the 10m tower level, and 1-min time series of wind speed at the 6 tower levels (10m, 20m, 40m, 80m, 140m, 200m).

Temperature criteria The detection algorithm used in the previous observational study to identify cold pool fronts by 1-min surface temperature is "designed to be sensitive to asymmetric cooling events visible in the time series, yet insensitive to high-frequency noise, to exclude false positives, and to group coincident fronts as one single event" [28]. We will build upon this algorithm. The steps implemented will be described here. The first step is to smooth the temperature time series with a running 11-min centered window. A series of threshold operations are then applied to the smoothed time series, to identify and "record" cold pool cases along with their properties:

1. A cold pool candidate is identified when the (smoothed) temperature is the minimum of a previous 20 minute window (the first T_{min}).

2. Contiguous minima are combined, if separated by 1 minute, or if within 20 minutes of each other given that the temperature does not exceed either of them by 0.5K. This way we avoid detecting the same cold pool more than once. We choose these values following the algorithm proposed in [28].

3. A temperature drop δT is defined as the difference between: the maximum (smoothed) temperature in the 20 minute time window before the first T_{min}, and the last T_{min} detected in the event. A time interval Δt is defined as the time elapsed between the first and last minima.

4. An event is recorded if δT exceeds a 1.5K threshold, and the time interval Δt does not exceed 60 minutes. The temperature threshold is raised compared to the one used in de Szoeke et al. 2017 [28] (aimed at detecting cold pools over a tropical oceanic surface). This was done to maintain the strongest cold pool signals, considering the higher temperature fluctuations over land than over the tropical ocean.

5. A stronger, refined temperature drop ΔT is defined as the difference between: the maximum unfiltered temperature within 10 minutes of the temperature drop , and the minimum unfiltered temperature within the temperature drop.

In figure 3.4 we see the temperature time series measured at 10 m of a specific day (August 27 2019), where an event was detected. We highlight here the first T_{min} and last T_{min} of the identified event.

Wind criteria A further criterion is then added to the detection algorithm, to ensure that there is a wind gust associated with each detected temperature decrease. For this scope, we use the time series of horizontal wind speed at the six tower levels. The horizontal wind speed is measured with vane anemometers that turn with the direction of the wind and record the velocity of the propellers. For each day we smooth the 1-min time series with a running 121-min centered window and subtract the smoothed time series from the original time series, to obtain the "horizontal wind anomaly". We choose the two-hour smoothing window to remove possible influences of the daily cycle. To strengthen the vertically coherent signals in the data set, we take the average wind speed of all six heights. This way, a wind gust visible in all six heights will rise above the noise. We call this variable the "height averaged horizontal wind anomaly" (Δu). For simplicity, we will name the maximum of this variable in a given time window "wind gust".

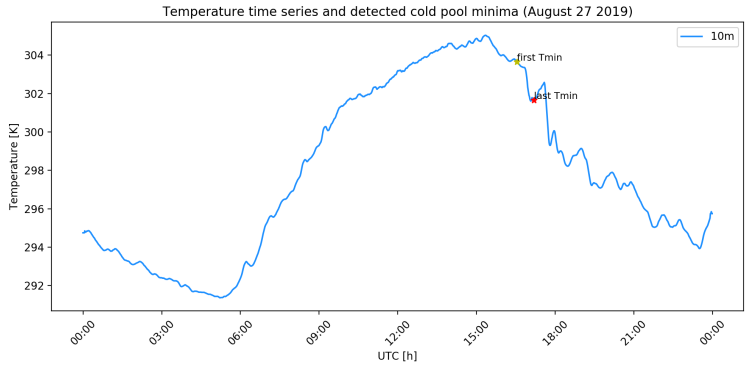

Figure 3.4: Example of the daily timeseries of temperature measured at 10m height and averaged over an 11-min centered smoothing window, and a temperature drop detected with the algorithm (August 27, 2019). The two stars indicate the first and last minima T_{min} of the event.

The detection algorithm then scans the events recorded thanks to the temperature criteria, and ultimately saves an event as a "cold pool" if there is a wind gust within 10 minutes of the time of the first T_{min} and the time of the last T_{min}, that exceeds 4 standard deviations (4σ) of the daily 1-min Δu time series. In figure 3.5 we see the height averaged horizontal wind anomaly time series of the same day shown previously (August 27, 2019). When values are above the dashed line, we know they are greater than 4 times the standard deviation of the daily wind anomaly. The peak seen in this figure, is the wind gust detected by the algorithm, related to the event detected by the temperature criteria.

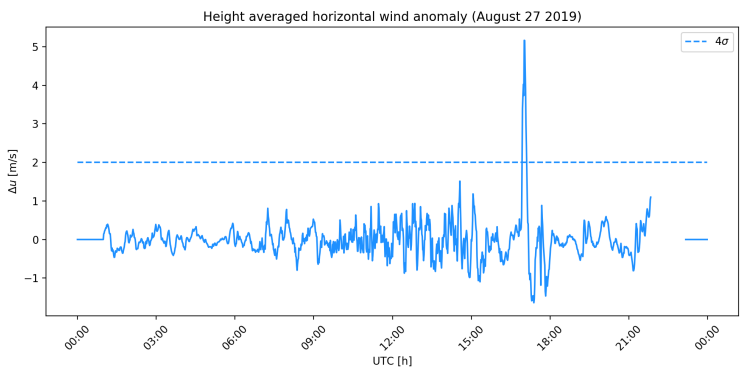

Figure 3.5: Example of the daily timeseries of height averaged horizontal wind anomaly (August 27, 2019). The dashed line indicates 4 standard deviations of the daily wind anomaly.

Chapter 4

Results and discussions

4.1 Case Studies

We first focus on two case studies, which are related by the fact that we are able to clearly see the gust fronts of the cold pools in the radar imagery. We aim to have a closer look at what happens specifically in the boundary layer when a cold pool gust front passes.

In the first case study we focus on a single cold pool that spreads almost perfectly centered around the Herwijnen radar tower. The unique location of this phenomenon enables us to visualize the evolution of the cold pool during the whole lifetime of the generating rain event.

In the second case study we focus on the interaction between three cold pool fronts, that collide almost perfectly above the Herwijnen radar. Thanks to this configuration, we are able to not only follow the evolution of the cold pools, but also to see what happens after their collision.

4.1.1 Isolated Cold Pool: August 27, 2019

The first case study is that of a cold pool generated by an isolated convective rain event which occurred nearly axisymmetrically around the Herwijnen radar tower on August 27, 2019. We were guided to look at this specific date by Michiel Baatsen and his keen memory for convective storms over the Netherlands. To understand the large scale atmospheric conditions we look at the nearest atmospheric sounding we could obtain, from the meteorological station in Essen, Germany, 135 km South-East of the Herwijnen radar tower. These soundings are available each day at 12:00 UTC, and they give us an approximate description of the atmosphere around the area of study. We see the skew-T diagram of the sounding in figure 4.1. The thicker left line indicates the dew point temperature at the various heights above the surface, and the thicker right line indicates the environmental temperature profile. The thin right-most line indicates the adiabatic path of a rising air parcel.

We firstly see that this was a very warm day for Northwestern Europe summer standards, as the measurement at the lowest recorded height (136m) reads 30°C. We also see that the lower troposphere is particularly dry, as the dew point depression (the difference between the temperature and the dew point temperature) at the lowest height is approximately 13 degrees, indicating that the lower tropospheric air is strongly under-saturated. We finally point out the CAPE (Convective Available Potential Energy) value, being 1433 J/kg. This is a measure of the amount of energy available for convection and corresponds to the area enclosed between the environmental temperature profile and the path of a rising air parcel (where the rising air parcel is warmer than the environment). Values above 1000 J/kg are favourable for the initiation of convective storms [34]. Overall, these characteristics are ideal for generating a convective cold pool: the high temperatures at the lowest levels can initiate convective motions due to heated surfaces. If precipitation events are formed due to the convective motions and high CAPE, the under-saturated lower troposphere will enable the evaporation of the rain to produce negative buoyancy and thus strong downdrafts.

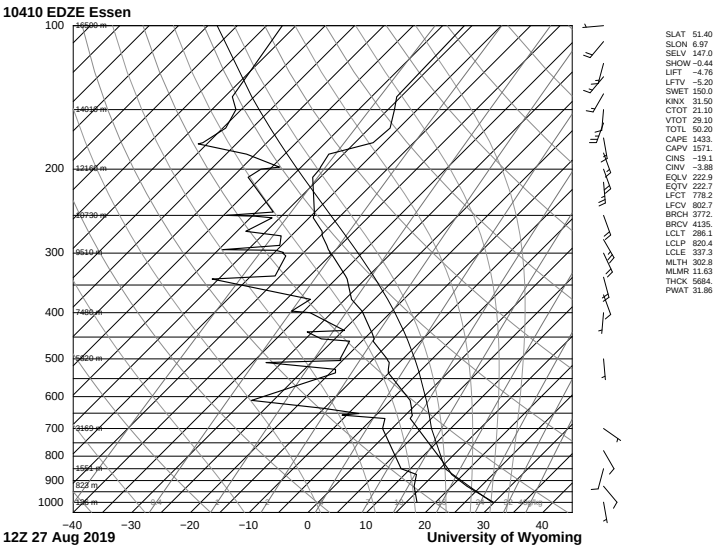

Figure 4.1: **Skew-T diagram of upper air sounding of the atmosphere above Essen, Germany, on August 27, 2019 at 12:00 UTC.** The left and right lines show respectively the dew point temperature and the temperature measured in degrees Celsius, at different heights. The height above the surface is shown on the y-axis in both pressure-coordinates (hPa) and in meters.

There would supposedly be a strong temperature gradient between the inside of these potential cold pools and the outside environment.

We look at the radar imagery of the precipitation field on this day and realize that in this event, gust fronts of a cold pool can be clearly seen in the reflectivity. In figures 4.2a - 4.2d we see the time evolution of the precipitation field and related cold pool on August 27 2019 around 17:00 UTC. On the left of figures 4.2a - 4.2d we show the reflectivity variable measured in dBZ at an angle of 1.20° from the horizontal, with a color bar fitted to highlight the lowest values. This way the gust fronts are highlighted and the strong rain generating events are shaded with a purple color. The circles show the height in km at which the radar beam is measuring. If approximating the cold pool with a circle in the reflectivity figures, its radius increases by 2 km every 5 minutes, which corresponds to a velocity of 6.7 m/s. On the right of figures 4.2a - 4.2d we show the radial velocity at which the particles in the air are moving. This variable is measured in knots, which can be divided by 2 to obtain the approximate value in the more common unit m/s. The gust front propagation velocity obtained before lies within the range of radial velocity values within the area of the cold pool (6-10 m/s) measured by the radar beam at various heights. We compare these values to the estimate of gust front propagation velocity obtainable with equation 2.1. We take $\Delta T = 3$ K, based on the surface temperature anomaly measured at Cabauw tower (see figure 4.4) and $T_0 = 304$ K based on the temperature value measured at Cabauw tower before the arrival of the gust front. To give a rough estimate of the cold pool depth, we check the radar imagery at different measurement angles, and notice that we loose any signal of the gust front in the reflectivity or the radially spreading air in the radial velocity between 500m and 1000m. If we take H = 750 m, we have an estimate of the propagation speed of c $\approx$ 8.5 m/s, which also lies in the range of the radial velocity values measured, although towards the higher end of the range.

We inspect the WOW-NL data (figure 4.3), to find evidence of the spatial change in temperature at the surface due to the spreading cold pool. We try to show three snapshots of approximately the same area shown in figure 4.2 and within the same time window. Gridded radar imagery showing precipitation intensity is superimposed to the WOW-NL temperature data. We see a gradual decrease in temperature directly below the precipitating event in figure 4.3a. We then notice that the surrounding stations also measure a decrease in temperature in the following time

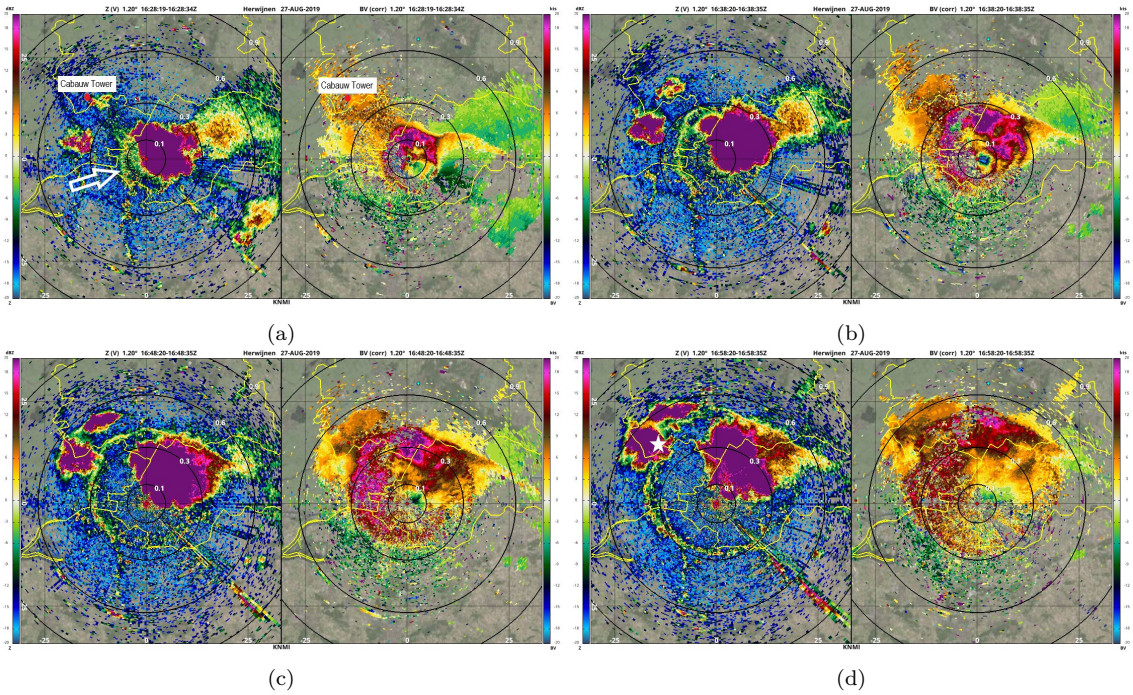

Figure 4.2: **Sequence of radar images of August 27 2019 cold pool, visualized with NLradar [31].** Snapshots are shown from 16:28 UTC (figure a) to 16:58 UTC (figure d), with 10 minute intervals between each image. The radar tower is in the center of each square. The black circles around the center indicate the height (in km) that the radar beam is measuring. The background grid lines indicate a horizontal length of 25 km. In the reflectivity images (left squares) we see a rain event (reflectivity>20 dBZ in purple) directly over the radar tower, and in the radial velocity images (right squares) we see radially spreading air (positive radial velocity in pink/purple colors) around the tower. The white arrow indicates the outer edge of a cold pool generated from the rain event, seen in the reflectivity. This outer edge corresponds to the radially spreading air seen in the Radial Velocity. We can follow the evolution of the cold pool gust front in both the reflectivity and radial velocity. The cold pool gust front passes the Cabauw tower shortly after figure d, as marked by the white star. There is also a new rain event developing over the Cabauw tower. The cold pool gust front is still visible in the Reflectivity and Radial Velocity after 40 minutes from the first image, at heights between 300 and 600 meters above the surface.

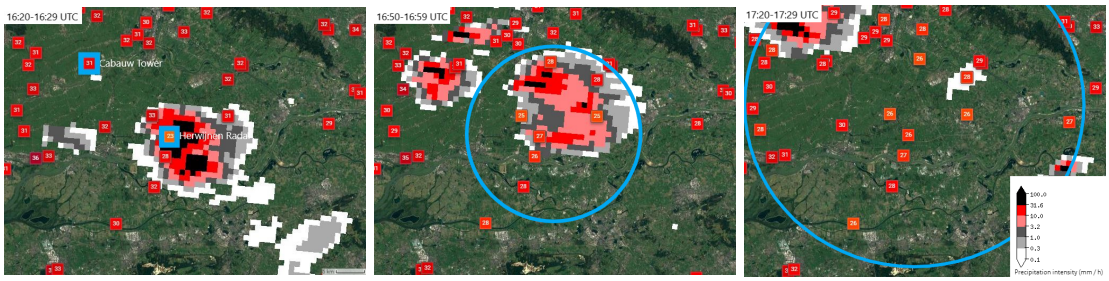

(a) (b) (c)

Figure 4.3: **Sequence of WOW-NL spatial temperature data with superimposed precipitation intensity from gridded radar imagery, from August 27 2019.** Snapshots shown from 16:20-16:29 UTC (figure a) to 17:20-17:29 UTC (figure c), with 30 minute intervals between subsequent images. Each WOW-NL station is represented by a square, containing the temperature measured (in Celsius) in the 10 minute time window indicated. The Herwijnen and Cabauw stations are highlighted with blue squares in figure a. A blue circle indicates the position of the gust front. We notice a gradual cooling of the surface air in the space around the precipitating event, and the colder temperatures persist in the area within the cold pool boundaries, also after the rain has stopped.

steps. This lower surface temperature lingers in space even after the rain event has dissipated.

We now focus on the measurements from Cabauw tower, to understand the specific signal of a passing cold pool gust front, and to obtain a clearer picture of the "interior" of the cold pool. In figure 4.4 we see the 10-minute time series of three variables measured at Cabauw tower at all tower heights: temperature, wind speed and specific humidity. We highlight with a red vertical line the time at which the maximum wind speed is measured at all tower levels. This time also corresponds to the time that the gust front in the radar reflectivity reaches the Cabauw tower. We see that around 10 minutes prior to that time, the temperature starts decreasing at all levels of the tower, with the lowest level (2m) going from being the warmest to becoming the coldest of all levels. The temperature anomaly ranges from 2 to 4 K depending on the tower level. We then see a gradual recovery of temperature at all levels. Note that sunset on this day is at 18:40 UTC, thus we see also the transition from an unstable diurnal boundary layer to a stable nocturnal boundary layer within the viewed time window. We see a clear peak in the horizontal wind speed measured at all levels of the tower, coinciding with the red line. The maximum wind speed increases with height. The maximum wind speed measured at the highest tower levels (6.3 m/s) is comparable to the propagation speed measured from the gust front in the radar reflectivity. We notice that the specific humidity drops at all levels after the red line, indicating that the cold pool contains drier air than the environment. The lowest two levels show an increase in humidity in the 20 minute time window preceding the red line. It is important to note that in the 20 minute window preceding the red line, there is a separate rain event above Cabauw tower, disconnected from the rain event that produced the cold pool in question. This rain event probably influences the measurements, perhaps contributing with its own downdraft to the decrease in temperature, increase in wind speed and changes in specific humidity produced by the initial cold pool.

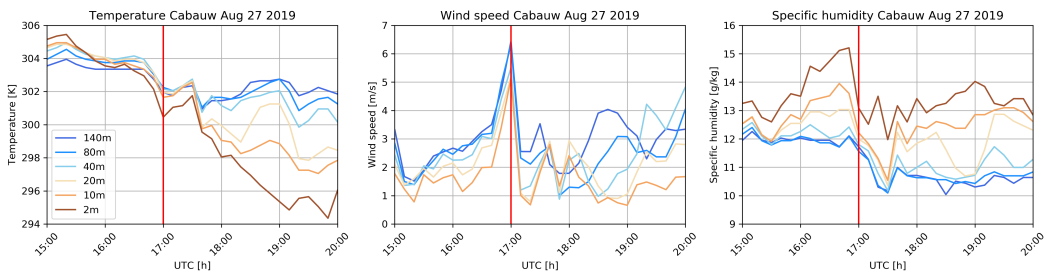

Figure 4.4: **Time series of temperature, wind speed and specific humidity measured at the various heights of Cabauw tower on August 27 2019.** The vertical red line indicates the time of maximum measured wind speed, which also corresponds to the approximate time that the gust front seen in the radar reflectivity reaches the Cabauw tower.

4.1.2 Cold Pool Collision: May 29, 2018

The second case study is that of an occasion in which several visible cold pools were generated by different convective rain events which occurred around the Herwijnen radar tower on May 29, 2018. The unique aspect of this case is that the gust fronts of the generated cold pools visibly collide, and the point of intersection happens to coincide with the radar tower. We are able to study the effect of the collision, namely the creation of a new rain event above the radar tower. We were guided to look at this specific date by Bram Van 't Veen, thanks to his close acquaintance with the KNMI radar imagery. To understand the large scale atmospheric conditions we again look at the atmospheric sounding from the meteorological station in Essen, Germany. The skew-T diagram of the sounding (figure 4.5) shows that this was a particularly warm day again, with the lowest recorded height (102m) reading about 28°C. The lower troposphere is also particularly dry, as the dew point depression (the difference between the temperature and the dew point temperature) at the lowest height is approximately 11 K, indicating that the lower tropospheric air is strongly under-saturated. The CAPE value is again high: 1294 J/kg. We can confirm the ideal characteristics for generating a (visible) convective cold pool seen in the first case study: high surface temperature, high CAPE and large dew point depression in the boundary layer.

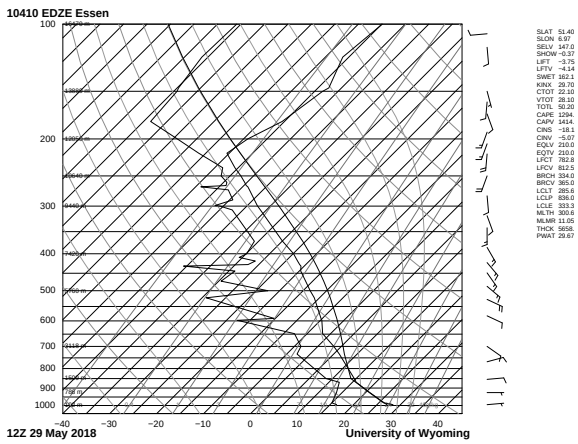

Figure 4.5: **Skew-T diagram of upper air sounding of the atmosphere above Essen, Germany, on May 29 2018 at 12:00 UTC.** The left and right lines show respectively the dew point temperature and the temperature measured in degrees Celsius, at different heights. The height above the surface is shown on the y-axis in both pressure-coordinates (hPa) and in meters.

The radar imagery of the precipitation field on this day provides observational evidence of a three-way cold pool collision leading to the formation of a new rain event. In figures 4.6a - 4.6f we see the time evolution of the precipitation field and related cold pools on May 29 2018 after 14:20 UTC. We decide to show the already formed gust fronts, from the time one of them passes above the Cabauw tower (figure 4.6a) to the moment they collide (figure 4.6d) and a new rain cell is formed (figure 4.6f). The left side of each figure shows the reflectivity measured in dBZ at an angle of 1.20° from the horizontal, with a color bar fitted to highlight the lowest values. We approximate the cold pools with circles in the figures, and observe the increase in radius of the circles within the 30 minute window prior to the collision. The gust front from the North-West (front 1 in figure 4.6a which hits Cabauw tower first) travels the fastest, at roughly 8 m/s, while the front from the North-East (front 2 in figure 4.6a) travels at roughly 6 m/s, and the front traveling from the South (front 3 in figure 4.6a which hits Cabauw tower after the collision) is the slowest, traveling at roughly 4 m/s. This difference in speeds might be related to the background wind speed: When observing the radar imagery over a longer time period, we see that the main upper-level wind field advecting the clouds is blowing from the South-East at approximately 5 m/s and this produces an environmental wind shear in the opposite direction of the propagation of front 1 and in the same direction of the propagation of front 3, possibly increasing the speed of front 1 and decreasing the speed of front 3. The right side of figures 4.6a - 4.6f shows the radial velocity at which the particles in the air are moving. We first see negative radial velocities in the range of 4-9 m/s corresponding to the three fronts approaching the radar tower. We try to estimate the gust front propagation velocity of front 1, with equation 2.1. We take $\Delta T = 7$ K, based on the temperature anomaly measured at the surface of the Cabauw tower during the passing of front 1 (see figure 4.8) and $T_0 = 302$ K based on the temperature measured at the Cabauw tower before front 1. We estimate H to be 750m since we again see loose the signal of the gust front in the reflectivity and the radially spreading air in the radial velocity between 500m and 1000m. With these values we obtain c $\approx$ 12 m/s. This estimated value is higher than the values found in the radar imagery. After colliding, the fronts seem to run through one another, and continue traveling each in their direction although they are less defined in the reflectivity. The front from the South (front 3) eventually hits Cabauw tower again (about 30 minutes after figure 4.6f).

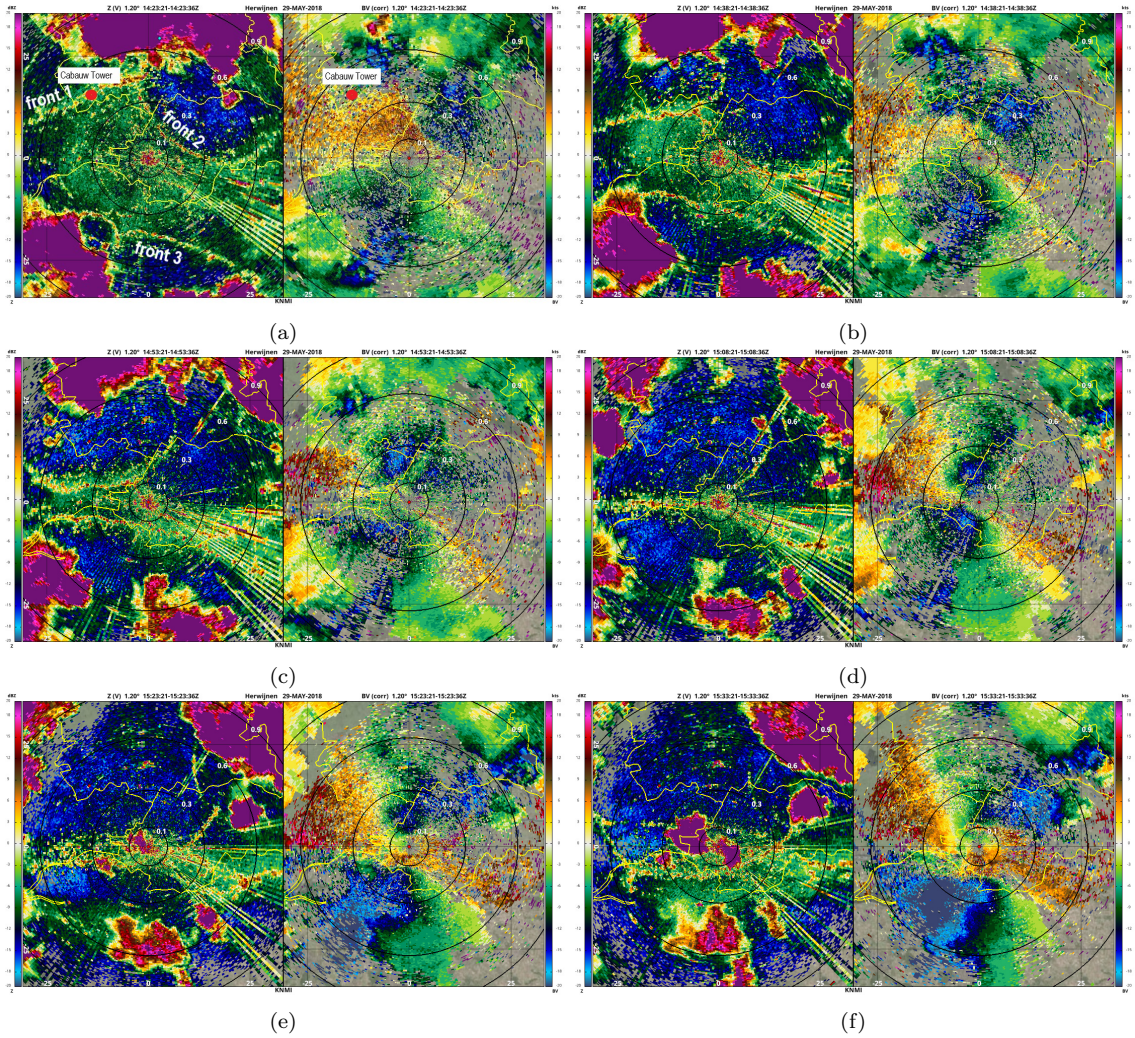

Figure 4.6: **Sequence of radar images of May 29 2018 cold pool collision, visualized with NLradar.** Snapshots are shown from 14:23 UTC (figure a) to 15:33 UTC (figure f), with 15 minute intervals between each image. In the reflectivity (left squares) we see various rain events (reflectivity>20 dBZ in purple) in the outer parts of the area, and developed cold pool gust fronts. The upper left gust front is above the Cabauw tower in figure a. In the radial velocity (right squares) we see that there is movement towards the radar tower (negative radial velocities in blue). In figure d, We see the gust fronts collide directly above the radar tower. We notice that a new rain event has formed in the point of collision above the radar tower in figure e. We also see the growth of the rain event generated by the colliding gust front and note that the collided gust fronts continue traveling, as we can see in both the reflectivity (left) and in the Radial Velocity (right) which shows radially positive velocities near the radar in figures e and f.

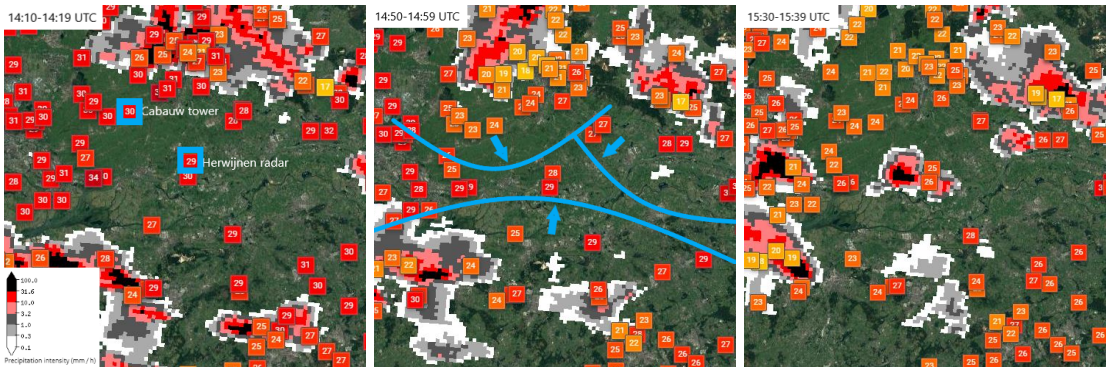

(a) (b) (c)

Figure 4.7: **Sequence of WOW-NL spatial temperature data with superimposed precipitation intensity from gridded radar imagery from May 29, 2018.** Snapshots shown from 14:10-14:19 UTC (figure a) to 15:30-15:39 UTC (figure c), with 40 minute intervals between subsequent images. Each WOW-NL station is represented by a square, containing the temperature measured (in Celsius) in the 10 minute time window indicated. The Herwijnen and Cabauw stations are highlighted with blue squares in figure a. We schematize the propagation of the cold pool gust fronts with blue lines and arrows. We notice a gradual cooling of the surface air in the space around the precipitating events, and the formation of a highly precipitating event above the Herwijnen station in the center of figure c.

We inspect the WOW-NL data (figure 4.7), to find evidence of the spatial change in temperatures at the surface due to the spreading cold pools. We want to confirm that the gust fronts seen in the radar imagery of figure 4.6, one of which produce a measurable temperature drop at the Cabauw tower, also correspond to a spatial cooling of the surface air. We visualize the data in figure 4.7 as similar as possible to figure 4.6, regarding spatial views and temporal window. We see the temperature measured at the various WOW-NL stations, and the precipitation intensity from gridded radar data. We see that all stations show a decrease in temperature from figure 4.7a to figure 4.7c, confirming that there is a spatial cooling connected with the gust fronts even in locations where there has not fallen rain. Note that the stations included in the WOW-NL do not measure temperature at the same time, but within the 10 minute time window indicated. Therefore, although two locations might experience a temperature drop at the same time, this might not be recorded in the figure showing the specific 10 minute time window.

We now focus on the Cabauw tower station, to see what happens specifically when the gust fronts pass the tower. Figure 4.8 shows the 10-minute time series of three variables measured at Cabauw tower at all tower heights: temperature, wind speed and specific humidity. We highlight with red vertical lines the time points in which the maximum wind speed is measured at all levels. These times correspond to the approximate time that the two successive gust fronts seen in the radar reflectivity (front 1 and front 3 in figure 4.6a) reach the Cabauw tower. We notice that both fronts bring a decrease in temperature, from 4 to 8 K depending on the height, with the lowest levels cooling the most with the passage of the first cold pool. We also see associated wind peaks in the horizontal wind speed at all levels, with the first front being the stronger. Front 1 also induces a wind shear which is not present before the arrival of the gust front. We notice that the measured wind speed at Cabauw related to front 1 is higher than the propagation speed calculated previously from the radar imagery. In other words, in this case the lower 140m of the cold pool head moves at a higher speed than the upper part of the head (which we assume to coincide with the updrafted particles which make the gust front visible at 500+ m in the radar imagery). Finally, there is a spike in specific humidity prior to the passage of the first front, preceding a net decrease in humidity at all levels, alluding to a possible moisture ring [29]. The second front however does not have a clear moisture signal. When looking at the wind direction data from the Cabauw tower

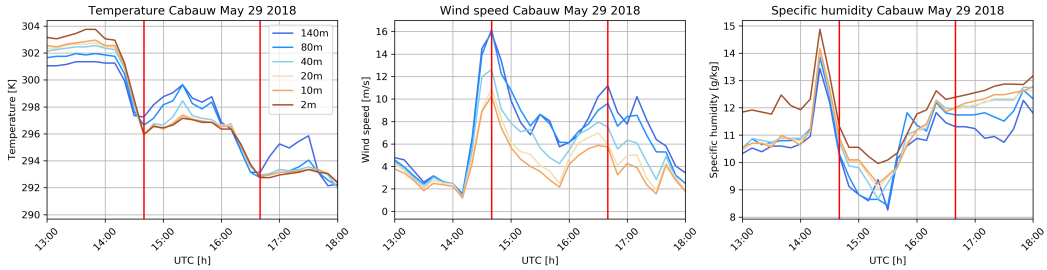

Figure 4.8: **Time series of temperature, wind speed and specific humidity measured at the various heights of Cabauw tower on May 29, 2018.** The time series are colored by the height of the tower at which they are measured, from 2m (brown) to 140m (dark blue). The vertical red lines indicate the times when the maximum wind speed is measured at all vertical levels. These times correspond to the approximate time that the two successive gust fronts seen in the radar reflectivity (front 1 and front 3 in figure 4.6a) reach the Cabauw tower.

(not in figure), we see that the first front comes from the North-West direction, and the second comes from the South-West, which suggests that the second temperature dip corresponds to the cold pool that was initially traveling from the South, and continued traveling after the collision. This second measured front is probably also fed by the new precipitating event above Herwijnen tower.

4.2 A Summer Study

We now expand the study in Section 4.1 which focused on specific cold pool cases, to the 5 month summer period of May-September 2019. For this time window we have 1-minute temporal resolution data of temperature and wind speed, along with high temporal resolution measurements of vertical wind and water vapor concentration from the Cabauw tower. This data enables us to have a more detailed view of what happens when a cold pool passes by the tower. We apply the algorithm for cold pool detection presented in the Methods (chapter 3), to the temperature and horizontal wind speed time series and examine the cases found. For each of the cases we look at the hi-res humidity and vertical wind speed data, and subsequently at the radar data to make a link with the generating rain events. We define the same time axis for all events, which has its origin (*time* t_0) at the time of the maximum horizontal wind speed anomaly. t_0 is defined to be able to compare the various events and to see how the other measured variables change with respect to the horizontal wind peak.

Discussion on detection criteria applied in the algorithm The temperature criteria used in this algorithm to detect cold pools were chosen initially based on the algorithm previously built for oceanic cold pools [28]. The temperature dip threshold of 0.5 K used in their algorithm was meant for detecting cold pool signals from tower measurements in a humid tropical oceanic environment. We therefore modified the algorithm and tuned the thresholds to the expected properties of cold pools over land in the midlatitudes. Simulation studies show that in drier environments like the locations of our study, cold pools are expected to be stronger (larger temperature drops and stronger wind gusts) than in humid environments like the location of the previous oceanic study where negative bouyancy production due to rain evaporation is more limited [17]. Considering this, we inspected the Cabauw temperature and wind time series related to the cold pools we could follow with the radar imagery, to get an idea of which possible temperature and wind values were realistic. We applied the algorithm initially to the summer of 2019. We included the wind gust criterion and raised both the wind gust and temperature thresholds until we were left with only the events that could be related to precipitation events. While we are knowingly missing weaker

cold pool cases this way, we have confidence that the cases remaining are indeed evaporatively driven cold pools.

We present three specific cold pool cases from the 18 cases detected by the algorithm over the summer of 2019 and successively we give an overview of all cases. The three cold pools we showcase, have a particularly clear signal and originate from different kinds of precipitating systems. Since we are not able to see the cold pool gust fronts in the radar reflectivity, we will show the radar imagery of the rain intensity of the generating rain events prior to the detected cold pool signal. The rain intensity is calculated by the radar visualizer [31] which interpolates the reflectivity variable at a height of 1.5 km and converts it using the Marshall-Palmer relation. In addition, we will show the time series of temperature, moisture anomaly and vertical wind speed superimposed upon the horizontal wind speed anomaly. The time axis Δt shows minutes relative to t_0. The temperature time series T are shown as measured at the various heights of the tower. The horizontal wind anomaly Δu is shown in grey in each figure as the "height averaged horizontal wind anomaly" explained in the Methods (chapter 3), and serves mostly as a time reference to compare each variable to. The remaining variables are not part of the detection algorithm, so their behaviour is independent of the criteria used to select the cold pools. In other words, what we see in the moisture, and the vertical wind, is independent from the temperature and horizontal wind criteria that we used to detect the single cases. The moisture anomaly Δq is shown as a difference from the 2-hour mean calculated from the preceding time window. We do this to specifically see if there is a net moistening around t_0, i.e. to see if there are moisture rings in the outer edge of the cold pool. The vertical wind w is shown as measured, and averaged over the three heights of the Cabauw tower containing sonic anemometers, to obtain a stronger signal. The averaging clearly removes some height information, but the vertical velocity measurements are quite noisy, so we give priority to having a strong signal.

Example of a cold pool from isolated rain event The first cold pool of the "summer collection" presented is from August 19, 2019. It is similar to the case of August 27, 2019 discussed in the previous case studies, as it also originates from an isolated convective event. Differently from the August 27 case, it does not rain directly above the radar tower when the gust front hits the tower (at Δt=0), so the measurements at the time of the passing gust front are not influenced by a secondary rain event and the high resolution measurements are "cleaner". In figure 4.9 we see the generating precipitating cell before the gust front is measured at the tower. In figure 4.10 we see the measurements taken at Cabauw tower before and after the gust front hits. In the temperature time series, we see that the lowest level (2m) is initially the warmest level, then descends to becoming the coldest level within 5 minutes of the gust front and then slowly recovers. The higher levels also measure a temperature drop, although not as strong (less than 2K temperature drop at 200m, compared to a 4K temperature drop at 2m and 10m), and with a quicker recovery. This is a good example of a signal that could be expected with the passing of the cold pool head: a temperature drop spanning all levels of the tower. The passing of the cold pool head is then followed by the interior of the cold pool, measured after t_0, which exhibits the cold downdraft air lingering at the lowest levels. In the moisture time series, we see a clear drying after t_0, but no obvious indication of a moisture ring. The vertical wind time series is noisy, but we distinguish an updraft shortly before the horizontal wind gust.

Example of cold pool from multiple rain events The second cold pool of the "summer collection" presented is from June 13, 2019. The rain field in this case is more complex, with more than one convective rain event contributing to the measurements, as we can see in figure 4.11. When observing the time series in 4.12 we see a wind gust coincide with a temperature drop in all levels at time 0 but the difference between lower levels and higher levels is not as obvious as the previous case. The moisture time series shows a drying, a quick recovery and a secondary drying, possibly due to the effect of downdraft air from the various rain events above the tower at and after t_0. The vertical wind speed here shows a very clear updraft slightly before t_0, as the previous

case, followed by a clear downdraft, giving indication of the measurable presence of a vortex ring in the leading edge of the cold pool.

Example of cold pool from organized linear rain event The last cold pool of the "summer collection" presented is from May 8, 2019. This cold pool is generated by an organized linear precipitating system, as we can see in 4.13 and although its origin is different from isolated summer convective events observable on a hot sunny day, the measured properties of the cold pool are similar to the previous: a drop in temperature coinciding with a wind gust, followed by dry interior, and especially a sharp updraft-downdraft dipole around t_0 (see 4.14). The major difference from the earlier cases, is seen in the temperature signal: when the gust front hits the Cabauw tower, all tower levels drop to nearly the same temperature, and quickly recover once the front has passed. It is debatable whether this kind of cold pool can be included in the general study of properties of cold pools originating from isolated convection. The measured properties of the fronts originating from larger-scale organized convective systems might in fact be characterized more by the large scale environmental properties than by the density current theory. The type of precipitating system might therefore be an extra dimension to consider when studying the various cases, as we will discuss later.

Composites of all summer 2019 cold pools We create composites of all 18 cases found in the summer of 2019, by averaging the various time series. We do this to have an overview of the measured properties of all the cold pools. We present the composites in the same order as the time series shown earlier. In figure 4.15 we show the composites of horizontal wind speed anomaly in grey, along with: temperature anomaly (measured at 10m, calculated with respect to the maximum temperature measured before in the 10 minutes before t_0), moisture anomaly (calculated as previously) and vertical wind. We see that overall, the composited cold pools exhibit a behavior similar to the three presented cases: a horizontal wind peak associated with a temperature drop, as a natural consequence of the detection algorithm, along with an average drying and a positive vertical wind peak before the horizontal wind peak. Although the updraft signal is quite clear in the composites, we loose any signal of a successive downdraft, probably due to the fact that the measured downdrafts of the different cold pool gust fronts occur at different times with respect to time 0, thus cancelling each other out. We have an average maximum height-averaged horizontal wind anomaly (calculated as previously) of 6 m/s, an average maximum temperature drop at 10m of 3K, an average maximum humidity anomaly of 3 g/m^3 and a maximum vertical updraft of 0.5 m/s shortly before the peak in horizontal wind. We also conclude that there is no clear signal of a moisture ring at or preceding time 0. Regarding time scale, on average, the temperature tends to not recover to its maximum value even after an hour has passed from the horizontal wind peak. The moisture content, however, tends to recover within an hour. Furthermore, the vertical wind peak is visible 2-3 minutes prior to the horizontal wind peak.

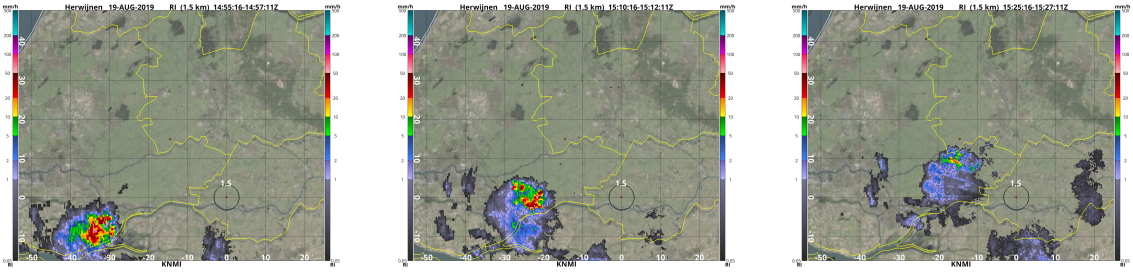

Δt = -30 min Δt = -15 min Δt = 0

Figure 4.9: Time sequence of rain intensity measured around the Herwijnen radar tower on August 19, 2019, visualized with NLradar [31]. The Cabauw tower is in the center of each image, marked by a red dot.

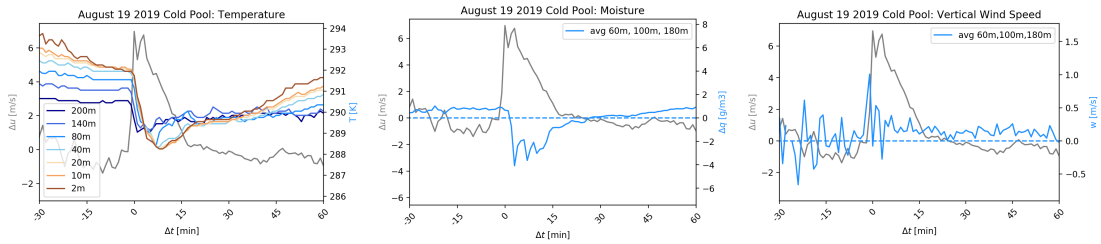

(a) (b) (c)

Figure 4.10: Time series of temperature (a), moisture anomaly (b) and vertical wind speed (c), superimposed on the horizontal wind anomaly (in grey), measured at Cabauw tower on August 19, 2019 before and after the passage of a cold pool gust front.

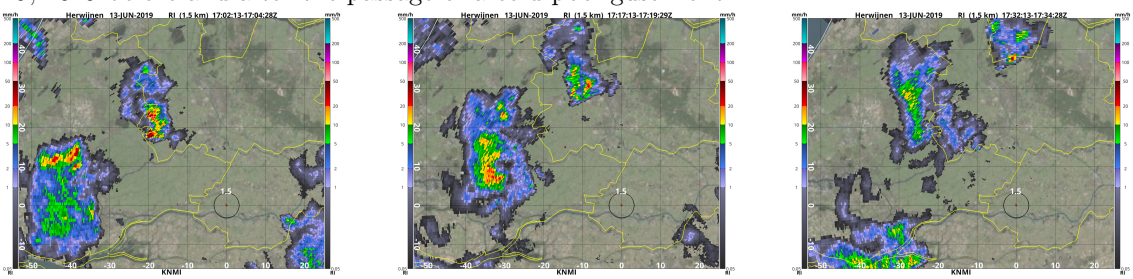

Δt = -30 min Δt = -15 min Δt = 0

Figure 4.11: Time sequence of rain intensity measured around the Herwijnen radar tower on June 13, 2019. The Cabauw tower is in the center of each image, marked by a red dot.

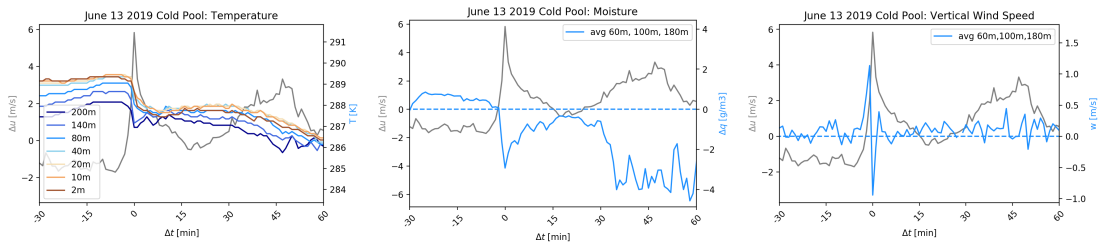

(a) (b) (c)

Figure 4.12: Time series of temperature (a), moisture anomaly (b) and vertical wind speed (c), superimposed on the horizontal wind anomaly (in grey), measured at Cabauw tower on June 13, 2019 before and after the passage of a cold pool gust front.

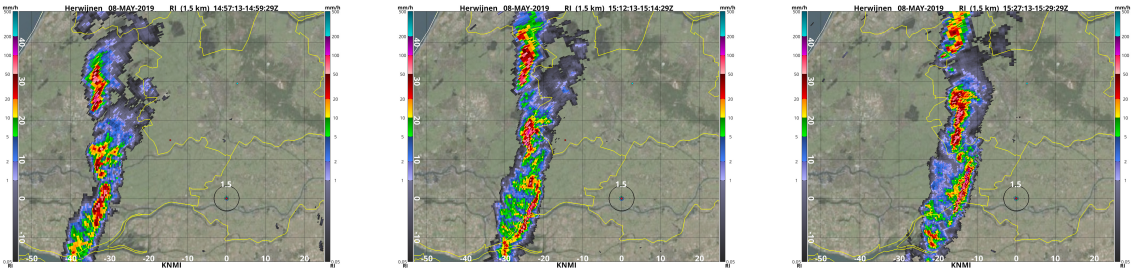

Δt = -30 min Δt = -15 min Δt = 0

Figure 4.13: Time sequence of rain intensity measured around the Herwijnen radar tower on May 8, 2019. The Cabauw tower is in the center of each image, marked by a red dot.

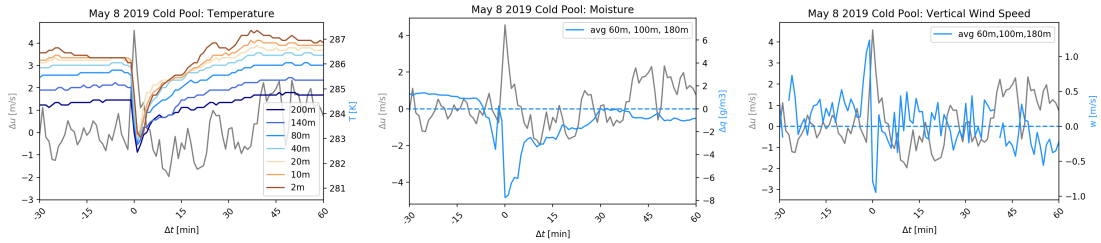

(a) (b) (c)

Figure 4.14: Time series of temperature (a), moisture anomaly (b) and vertical wind speed (c), superimposed on the horizontal wind anomaly (in grey), measured at Cabauw tower on May 8, 2019 before and after the passage of a cold pool gust front.

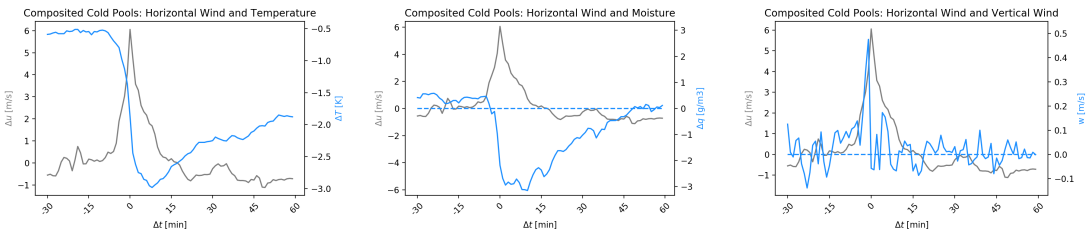

(a) (b) (c)

Figure 4.15: Composites of summer 2019 cold pools: Time series of temperature anomaly (a), moisture anomaly (b) and vertical wind speed (c), superimposed on the horizontal wind anomaly (in grey). 18 cold pool time series are averaged to create these composites.

Properties of all summer 2019 cold pools We now present the properties of all the cold pools found in the summer, to have an idea of the general values measured and to look for links between certain properties of the cold pools, the generating rain events, and the environmental conditions. Each case will be represented by a point based on its measured properties, and will be distinguished by its date of occurrence (day/month). By visual inspection of the radar imagery, we try to pinpoint which cold pool cases originate from isolated convection (where we can visually outline the generating rain event), and which cold pool cases originate from larger scale organized systems (mesoscale convective systems), possibly related to large-scale cold fronts. We label the isolated convection cold pools as "IC" (blue points) and the other systems as "OTHER" (grey points).

1. *Cold pool properties:*

   We start with defining specific cold pool properties to characterize our cases in the simplest way possible. Δu_{max} is the measured maximum height-averaged horizontal wind anomaly (the "wind gust" as defined in the methods section). ΔT is the refined temperature drop measured at 10 meters (as defined in the methods section). w_{max} is the maximum vertical wind speed measured at 60m in a 15 minute time window around time 0. In figure 4.16 we show these properties, with respect to one another. Intuitively, a "strong" cold pool is defined by a large Δu_{max} and a large ΔT. In figure 4.16a we get a general idea of the Δu_{max} and ΔT values calculated for each case and thus the "strength" of the cold pools. We wish to remind that we artificially cut off the cold pools with the lowest values of these two specific properties due to the algorithm criteria. In figure 4.16b we try to look at the internal structure of the so called vortex rings in the leading edge of the cold pools, to see which magnitude of horizontal wind gusts (Δu_{max}) correspond to which magnitude vertical updrafts (w_{max}). Intuitively a higher w_{max} is linked to a higher Δu_{max}. It is worth noting that these properties also depend on how far the originating precipitating event was from the Cabauw tower when the gust front was detected, i.e. at what point of its "life" we are measuring the cold pool. This adds another potential dimension to the study. We also note that the 5/6 case is always an outlier in the figures that include Δu_{max}. This higher than average value of horizontal wind could be due to external forcings, for example strong winds from higher altitudes being fed into the front through the large convective system.

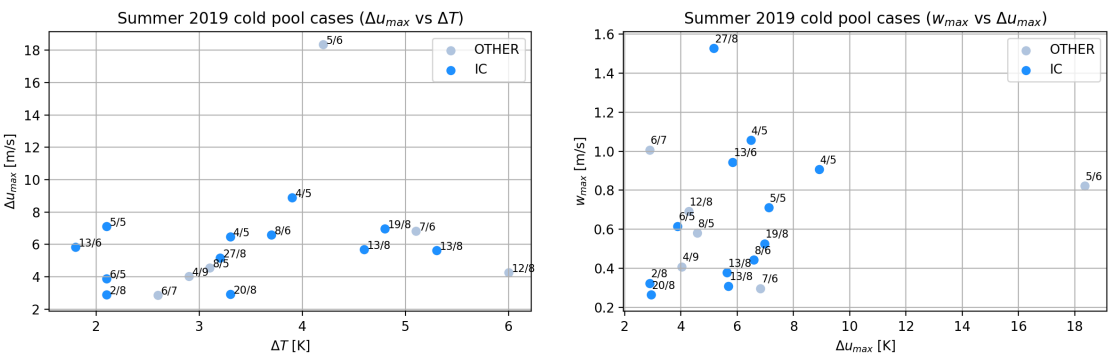

(a) (b)

Figure 4.16: **Summer 2019: Cold pool properties.** Each point represents a specific cold pool case according to its properties Δu_{max}, ΔT, and w_{max}. Each case is labelled according to the date in which it was detected, and colored according to the classification of its generating precipitation field (IC refers to Isolated Convection and OTHER refers to other larger scale precipitating systems).

2. *Cold pool properties vs. environment (atmospheric moisture)* After having defined the cold pool properties with respect to one another, we try to see how the main properties link with the characteristics of the environment, which we simplistically define with how saturated the lower atmosphere is. An approximation of the atmosphere's degree of saturation is the dew point depression, which we mentioned when observing the soundings relative to the case studies. A larger dew point depression is an indication of a dryer environment, while a dew point depression nearing 0 K is an indication of a nearly saturated environment. We calculate the average dew point depression $\bar{T} - \bar{T}_d$ by calculating the difference between the average temperature and dew point temperature measured at 140m (close to the lowest level of an atmospheric sounding). In figure 4.17 we look at the dependence of the two cold pool properties ΔT and Δu_{max} on the average dew point depression. Intuitively, the less saturated the atmosphere, the more rain can evaporate, consequently producing more cold air. This could hypothetically lead to a larger air density difference between the cold pool and the surrounding environment, thus producing a stronger horizontally spreading current (and higher horizontal wind gust values). We also note that the 5/6 case is again an outlier in figure 4.17b, showing a very strong wind gust connected to a low dew point depression, indicating again that the wind intensity is probably due to external factors related to the mesoscale system rather than the local conditions.

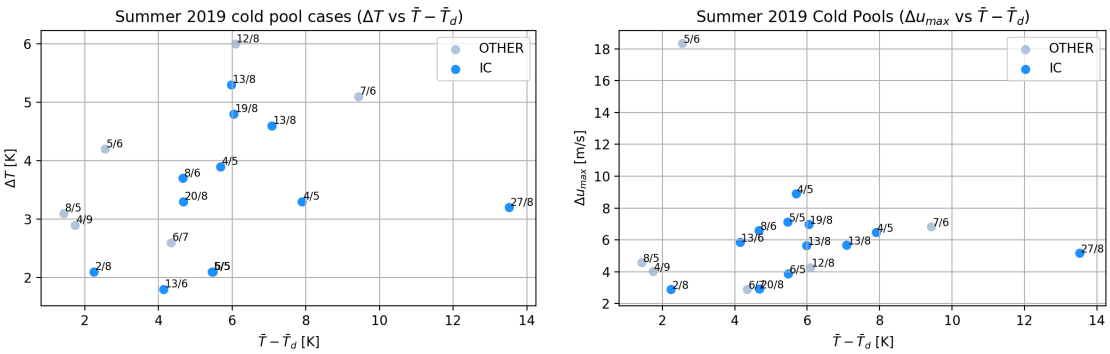

(a) (b)

Figure 4.17: **Summer 2019: Cold pool properties vs. environment (atmospheric moisture).** Each point represents a specific cold pool case according to its properties ΔT and Δu_{max} against the environmental dewpoint depression $\bar{T} - \bar{T}_d$. Each case is labelled according to the date in which it was detected, and colored according to the classification of its generating precipitation field (IC refers to Isolated Convection and OTHER refers to other larger scale precipitating systems).

3. *Cold pool properties vs. rain intensity:* We finally try to make a link between the cold pool properties and the rain intensity of the generating rain cell. We do this by visually inspecting the radar imagery of each case, and finding the maximum radar-derived rainfall intensity within the rain event we hypothesize to be the generating rain cell, 15 minutes before the cold pool gust front is detected at the Cabauw tower. In figure 4.18 we show the cold pool properties ΔT and Δu_{max} with respect to the maximum rainfall intensity RI_{max}. Intuitively, the higher the rainfall intensity, the stronger the cold pool. If we look at figure 4.18a, there are some cases that do not follow this intuitive reasoning, namely 7/6 which reports an above average temperature drop connected to a relatively low rain intensity, and 2/8 which reports a low temperature drop connected to a high rain intensity. When we locate these cases in the previous figure regarding atmospheric moisture (figure 4.17), we see that 7/6 has one of the highest dew point depressions, indicating that the above average temperature drop might have been influenced more by the atmospheric dryness rather than the rainfall intensity. On the other hand, 2/8 has one of the lowest dew point depressions,

indicating a highly saturated atmosphere. This might have inhibited the evaporation of the rain, leading to a weak cold pool from a particularly intense rain event. Figure 4.18b suggests that rain intensity does not determine the strength of the gusts.

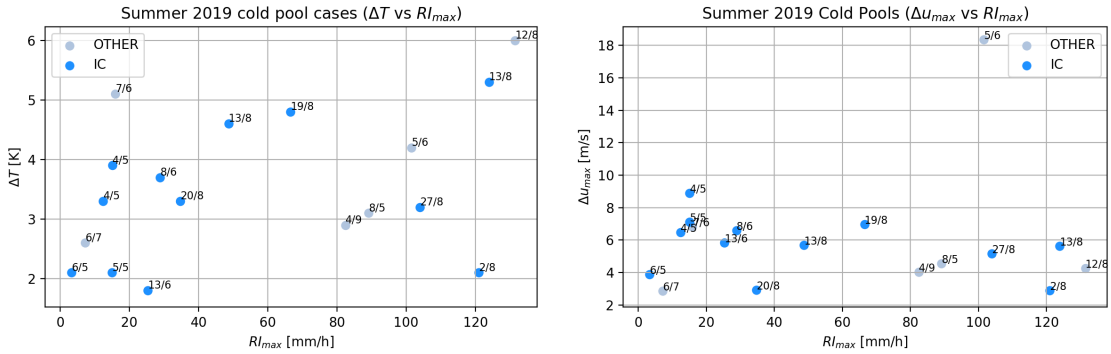

(a) (b)

Figure 4.18: **Summer 2019: Cold pool properties vs. rain intensity.** Each point represents a specific cold pool case according to its properties ΔT and Δu_{max} against the maximum rain intensity of the generating rain event RI_{max}. Each case is labelled according to the date in which it was detected, and colored according to the classification of its generating precipitation field (IC refers to Isolated Convection and OTHER refers to other larger scale precipitating systems).

4.3 A 15 Summers Study

Since we have 1-minute time series of temperature, wind speed and dew point temperature from the Cabauw tower extending back to 2005, we apply the detection algorithm to the time series from 15 summers (May-September 2005 to 2019). In figure 4.19 we give an overview of the time stamps in which we measure each of the 286 cold pool cases. Half of the cases detected are between noon and 18, with a peak in the three hours after noon, as one might expect from convection driven phenomena. We can now further inspect the link between the cold pool properties ΔT and Δu_{max}, and between these and the environmental saturation $\bar{T} - \bar{T}_d$. With many more data points we are able to see if statistical correlations arise between the properties.

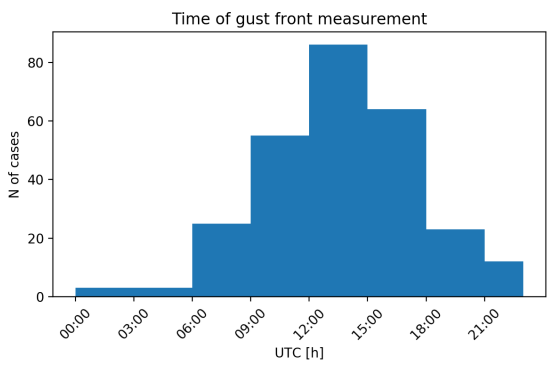

Figure 4.19: 15 summers study: histogram of time stamps of cold pool gust front measurement. Local summer time is UTC+2.

1. *Cold pool properties:* We look at the relation between the two cold pool properties ΔT and Δu_{max} with the extended data set in figure 4.20. We have 286 points corresponding to the cases found throughout the 15 summers with the same algorithm and criteria as used for the summer of 2019. We decide to calculate a linear fit to the visually correlated properties ΔT and Δu_{max} with a simple linear regression and obtain a positive angular coefficient. We calculate the Pearson correlation coefficient and obtain a value of ρ=0.51, indicating a moderate positive correlation between Δu_{max} and ΔT. This seems evident to the eye especially for the higher ΔT values (above 4K). The p-value for this correlation is in the order of 10^{-20} so we can attribute a high statistical significance to this positive correlation. We then test the relation suggested by 2.1, and use a non-linear least squares to fit the function $y = \sqrt{kx}$ to the data. We see that there are a few clear outliers from both functions with higher than average Δu_{max} values. One of these is the 5/6 case from the summer of 2019, from a gusty mesoscale convective system. We can hypothesize the other outliers to be from systems of this sort, influenced by factors external to the formation of the density current itself. Based on this figure, we can say that the two properties Δu_{max} and ΔT are a good measure of the "strength" of a cold pool, with a strong cold pool defined with higher values of both. It is interesting to find such a "simple" relationship between cold pool properties considering the complexity of the system which generates each cold pool, the many environmental factors that determine the properties, and the fact that we are measuring each cold pool at a different stage of its development. In figure 4.21 we show the same as the previous figure, but putting the cases into 5 year bins, to differentiate the more recent cold pool cases from the older cases. We curiously point out that the cases reaching the further right side of the figure (larger temperature dips and higher measured wind gusts) are all from the most recent 5 year bin, a part from one outlier. We applied the same algorithm with the same criteria to all the years, to time series from the same measurement tower. We don't know if any significant changes have been made to the measurement instruments, potentially changing their sensitivity, so we refrain from making any statement regarding the climate, but we leave the question open of how cold pool properties might be changing in a changing climate, to studies of potentially longer time spans.

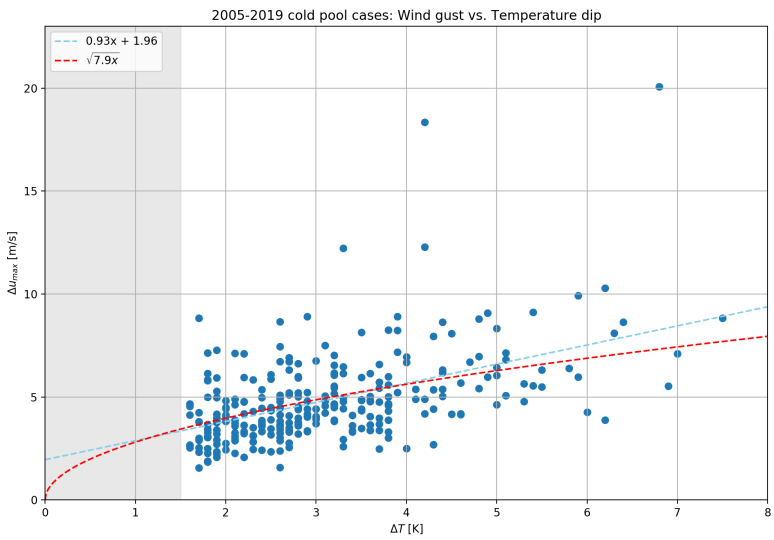

Figure 4.20: **15 summers study (2005-2019): Cold pool properties.** Each point represents a specific cold pool case according to its two properties Δu_{max} and ΔT. Shaded in grey is the area where we do not have cases due to the temperature anomaly threshold in the detection algorithm. The blue and red dashed lines are two different functions fitted to the data.

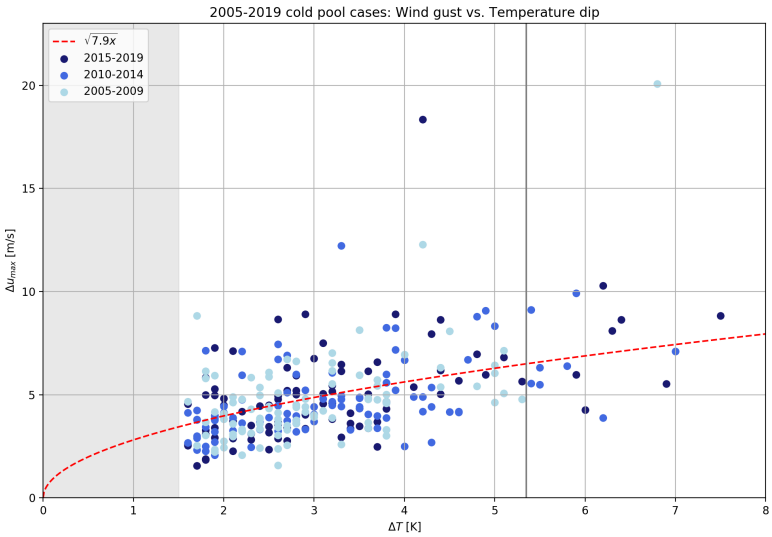

Figure 4.21: **15 summers study (2005-2019): Cold pool properties, with cases subdivided into 5 year bins.** Each point represents a specific cold pool case according to its two properties Δu_{max} and ΔT, and is colored based on which 5-year bin it belongs to. Shaded in grey is the area where we do not have cases due to the temperature anomaly threshold in the detection algorithm. We draw a vertical grey line to highlight that there is only one point from the 2005-2009 bin to the right of it, possibly suggesting that the strongest cold pools have been measured in the more recent years.

2. *Cold pool properties vs. environment (atmospheric moisture)* We look at the relation between the cold pool property ΔT and the atmospheric dew point depression $\bar{T} - \bar{T}_d$ with the extended data set in figure 4.22. We see that the dependance of cold pool strength on the environmental properties is a clearly less defined relationship than the connection between two internal properties of the cold pools. We calculate the Pearson correlation coefficient and obtain a value of ρ=0.2 and a p-value in the order of 10^{-3}. The correlation is still positive and statistically significant, but both statements are much weaker than in the previous figure. The light positive correlation suggests that a higher dew point depression (thus a larger dew point depression) is connected to larger temperature dips. We notice that for the lower dew point depressions (below 6 K), there seems to be a limit above which the measured temperature dip cannot be located. This is interesting, as it means that if the atmosphere is saturated enough, it is not possible to produce cold pools above a certain strength. On the other hand, at lower saturation values (higher dew point depression) it is possible to measure weak and strong cold pool signals, modulated by the other factors such as precipitation intensity and what stage of the cold pool we are measuring.

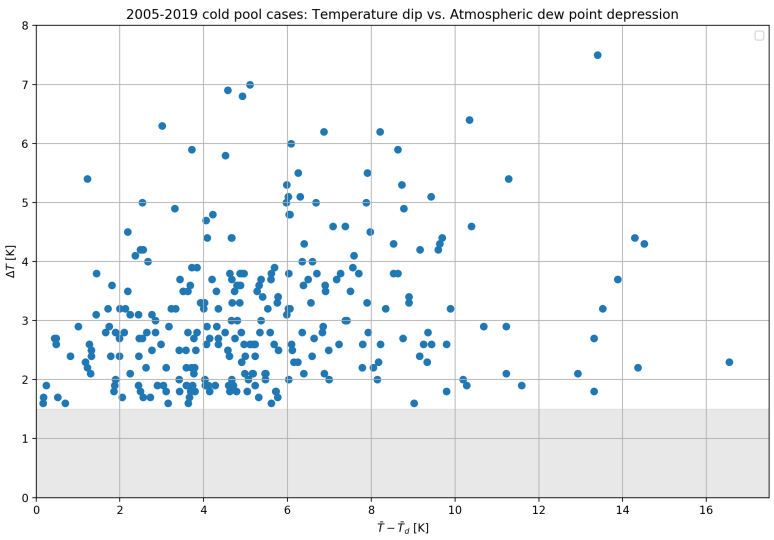

Figure 4.22: **15 summers study (2005-2019): Cold pool properties vs. environment (atmospheric moisture).** Each point represents a specific cold pool case according to its property ΔT, against the environmental dewpointdepression $\bar{T} - \bar{T}_d$. Shaded in grey is the area where we do not have cases due to the temperature anomaly threshold in the detection algorithm.

Chapter 5

Conclusions and outlook

In this thesis we have explored the phenomenon of evaporatively driven convective downdrafts (cold pools), through the use of meteorological observations. We first present two case studies consisting of two unique occasions within the last two years where the gust fronts of the cold pools were clearly visible throughout their life cycle in the radar reflectivity and velocity fields. One case consists of a cold pool developing and spreading concentrically around the (Herwijnen) radar tower, and the other consists of three large cold pool fronts colliding directly above the radar tower and producing new precipitation. In both cases, the gust fronts of the cold pools "hit" the (Cabauw) boundary layer measurement tower at a certain stage of their development. We use various data sources to understand the full meteorological situation and then to study the properties of the cold pools. To look at the *vertical* dimension of the atmosphere at high altitudes we use soundings obtained from the closest sounding-providing station in Essen. To look at the *horizontal* dimension of the atmosphere in the lower troposphere we use radar imagery, with which we visually see the gust fronts of the spreading cold pools and the precipitation field. To look at the *vertical* dimension of the lower boundary layer we use data from the 213m boundary layer measurement tower at Cabauw, which enables us to study the signal produced by a passing cold pool before, during, and after the gust front hits the tower. To look at the *horizontal* dimension of the temperature field at the surface we use WOW-NL. From both cases, each unique in its own way, we find a similar signal connected with the passage of the gust fronts: a drop in temperature (both vertically and horizontally in space), a peak in horizontal wind speed, and a drop in the moisture content at all tower levels.

With the first two properties in mind, we develop an algorithm to detect other cases from time series, and apply this to the summer of 2019. We confirm that each case detected actually originated from precipitating events in the surroundings of the Cabauw tower, thanks to the radar imagery. We study the high temporal resolution data of the various cases to look for evidence of two specific phenomena: moisture rings and the vortex ring in the leading edge of the cold pool. We don't find clear evidence of moisture rings measured around the time of the gust fronts, but we do see the updraft-downdraft dipole possibly indicating the passing vortex ring. In the composites we get an idea of the average characteristics of our cold pools, including the time scale of recovery. We see that the moisture content of the lower boundary layer tends to recover faster than the temperature, and we see a clear updraft signal preceding the gust front also in the composited vertical velocities. We then look at the general properties of the cold pools and the environmental properties in relation to one another, to have a better idea of what might influence the cold pool properties. We look for confirmation of the simplistic hypothesis that a highly unsaturated boundary layer and high rain intensity produce strong cold pools. By observing the figures we understand that the relations are not so simple, and that there are other degrees of freedom influencing the cold pool properties, which might be connected to the larger-scale synoptic properties of the atmosphere, and the specific type of precipitating system that generates the measured cold pool. When we look at the same relations, and add 14 more summers of data to the cases of 2019, a more defined correlation arises between the cold pool properties describing

the cold pool strength.

This study could be expanded in a number of ways. It is conveniently based on meteorological data from a boundary layer measurement tower and radar imagery, both of which can be found in long time windows and possibly in other places in the world. The detection algorithm can be applied to any meteorological tower data set containing 1-min measurements of temperature and horizontal wind speed. One could reproduce the study in other environments (e.g. oceanic vs. continental, at different latitudes, with different land moisture conditions) to better understand the influences of the environmental conditions on the cold pool properties. We have wondered about what conditions are necessary for the gust fronts to be visible in the radar imagery since it rarely occurs in our cases, but we have not come with a clear answer. A hypothesis is that, for dust and insects to be swept up to the necessary heights, we need particularly dry conditions. We wonder if this means that the fronts are not visible over an oceanic surface. One could also look further into the connection between rain intensity and cold pool properties. A suggestion would be to track the generating rain cells in the radar imagery, and correlate the accumulated rainfall intensities of these with the measured properties of the cold pools. If the selection of the most probable generating rain cell were automated, as opposed to being selected by visual inspection as in our summer 2019 study, it would be possible to look at this relation for all the cases of the 15 summers. It would be interesting to integrate this study with a look at the influence of passing cold pools on surface fluxes (sensible and latent), which remains an open question currently investigated. A final suggested investigation, with longer data series in time, would be to connect the phenomenon of cold pools to a changing climate, to see if the properties of these have changed over time along with the properties of their generating convective rain cells. This, in the bigger picture, might lead to a deeper understanding of how cold pools might contribute differently to the organization of convection in a changing climate.

Bibliography

[1] Cesar (cabauw experimental site for atmospheric research) database. https://ruisdael-observatory.nl/cesar-database/pages/datasetsKDC.html. Accessed: 2020-08-01. 11

[2] Knmi (koninklijk nederlands meteorologisch instituut) data platform. https://dataplatform.knmi.nl/catalog/index.html. Accessed: 2020-08-01. 10

[3] Wow-nl. https://wow.knmi.nl/. Accessed: 2020-08-01. 11

[4] C. D. Ahrens. *Meteorology Today*. Cengage Learning, 2008. 4, 10

[5] C. S. Bretherton, P. N. Blossey, and M. Khairoutdinov. An energy-balance analysis of deep convective self-aggregation above uniform sst. *Journal of the Atmospheric Sciences*, 62:4273–4292, 2005. 2

[6] S. J. Böing, H. J. J. Jonker, A. P. Siebesma, and W. W. Grabowski. Influence of the subcloud layer on the development of a deep convective ensemble. *J. Atmos. Sci.*, 69:2682–2698, 2012. 7

[7] C. Cafaro and G. Rooney. Characteristics of colliding density currents: A numerical and theoretical study. *Quarterly Journal of the Royal Meteorological Society*, 144, 06 2018. 2

[8] J. Charba. Application of gravity current model to analysis of squall-line gust front. 1974. 4

[9] A. J. Drager and S. C. van den Heever. Characterizing convective cold pools. *J. Adv. Model. Earth Syst.*, 9:1091–1115, 2017. 2, 6

[10] Z. Feng, S. Hagos, A. K. Rowe, C. D. Burleyson, M. N. Martini, and S. P. de Szoeke. Mechanisms of convective cloud organization by cold pools over tropical warm ocean during the amie/dynamo field campaign. *Journal of Advances in Modeling Earth Systems*, 7(2):357–381, 2015. 2, 7, 8

[11] M. Fournier and J. O. Haerter. Tracking the gust fronts of convective cold pools. *Journal of Geophysical Research: Atmospheres*, 124, 09 2019. 2

[12] J. O. Haerter. Convective self-aggregation as a cold pool driven critical 1 phenomenon 2. *Geophysical Research Letters*, 03 2019. 2

[13] J.O. Haerter, S. J. Böing, Henneberg O., and S. B. Nissen. Reconciling cold pool dynamics with convective self-organization. *arXiv: Adaptation and Self-Organizing Systems*, 2018. 2

[14] O. Henneberg, B. Meyer, and J. O. Haerter. Particle-based tracking of cold pool gust fronts. *Journal of Advances in Modeling Earth Systems*, 12(5), 2020. 7

[15] N. Jeevanjee and D. M. Romps. Convective self-aggregation, cold pools, and domain size. *Journal of the Atmospheric Sciences*, 40, 2013. 2

[16] J. B. Klemp, R. Rotunno, and W.C. Skamarock. On the dynamics of gravity currents in a channel. *Journal of Fluid Mechanics*, 269:169–198, 1994. 5

[17] M. J. Kurowski, K. Suelj, W. W. Grabowski, and J. Teixeira. Shallow-to-deep transition of continental moist convection: Cold pools, surface fluxes, and mesoscale organization. *Journal of the Atmospheric Sciences*, 75:4071–4090, 2018. 22

[18] W. Langhans and D. Romps. The origin of water vapor rings in tropical oceanic cold pools. *Geophysical Research Letters*, 42:7825–7834, 09 2015. 3

[19] P. Linden and J. Simpson. Microbursts: a hazard for aircraft. *Nature*, 317:601–602, 1985. 2

[20] P. Markowski and Y. Richardson. *Mesoscale Meteorology in Midlatitudes: Appendix A (Radar and Its Applications)*. Wiley, 2010. 3, 10

[21] P. Markowski and Y. Richardson. *Mesoscale Meteorology in Midlatitudes: Chapter 14 (Thunderstorms)*. Wiley, 2010. 2, 4, 5

[22] P. Markowski and Y. Richardson. *Mesoscale Meteorology in Midlatitudes: Chapter 5 (Outflow Boundaries)*. Wiley, 2010. 3, 5, 6

[23] T. Maxworthy, J. Leilich, J. E. Simpson, and E. H. Meiburg. The propagation of a gravity current into a linearly stratified fluid. *Journal of Fluid Mechanics*, 453:371–394, 2002. 5

[24] C. K. Mueller and R. E. Carbone. Dynamics of a thunderstorm outflow. *Atmos. Sci.*, 44(15):1879–1898, 1987. 2

[25] R. Rotunno, J. Klemp, and M. Weisman. A theory for strong, long-lived squall lines. *Journal of The Atmospheric Sciences*, 45:463–485, 1988. 3

[26] J. E. Simpson. *Gravity currents: In the Environment and the Laboratory*. E. Horwood, 1987. 6

[27] J. E. Simpson and R. E. Britter. The dynamics of the head of a gravity current advancing over a horizontal surface. *Journal of Fluid Mechanics*, 94(3):477–495, 1979. 5

[28] S. P. de Szoeke, E. D. Skyllingstad, P. Zuidema, and A. S. Chandra. Cold Pools and Their Influence on the Tropical Marine Boundary Layer. *J. Atmos. Sci.*, 74:1149–1168, 2017. 2, 12, 22

[29] A. M. Tompkins. Organization of tropical convection in low vertical wind shears: The role of cold pools. *Atmos. Sci.*, 58(2):1650–1672, 2001. 3, 8, 21

[30] G. Torri, Z. Kuang, and Y. Tian. Mechanisms for convection triggering by cold pools. *Geophysical Research Letters*, 42, 02 2015. 7, 8

[31] B. van 't Veen. Nlradar. `https://www.weerwoord.be/m/2429671`. Accessed: 2020-08-01. 10, 16, 23, 25

[32] R. Vogel. *The influence of precipitation and cconvective organization on the structure of the trades*. PhD thesis, Max-Planck-Institut für Meteorologie, Hamburg, 2014. 2

[33] R. M. Wakimoto. The Life Cycle of Thunderstorm Gust Fronts as Viewed with Doppler Radar and Rawinsonde Data. *Monthly Weather Review*, 110:1060–1082, 1982. 2, 3, 6, 7

[34] M. Weisman and J. Klemp. The dependence of numerically simulated convective storms on vertical wind shear and buoyancy. *Monthly Weather Review*, 110, 06 1982. 14

[35] M. L. Weisman and R. Rotunno. A theory for strong long-lived squall lines: Revisited. *Journal of the Atmospheric Sciences*, 61:361–382, 2004. 2

[36] A. A. Wing, K. Emanuel, C. E. Holloway, and C. Muller. *Convective Self-Aggregation in Numerical Simulations: A Review*, pages 1–25. Springer International Publishing, Cham, 2018. 2

[37] G.S. Young, S. M. Perugini, and Fairall C. W. Convective wakes in the equatorial western pacific during toga. *Monthly Weather Review*, 123:110–123, 1995. 2

[38] E. J. Zipser. Mesoscale and convective–scale downdrafts as distinct components of squall-line structure. 1977. 2

[39] P. Zuidema, Z. Li, R. Hill, L. Bariteau, B. Rilling, C. Fairall, W. Brewer, B. Albrecht, and J. Hare. On trade wind cumulus cold pools. *Journal of Atmospheric Sciences*, 69:258–280, 01 2012. 2

[40] P. Zuidema, G. Torri, and C. Muller. A survey of precipitation-induced atmospheric cold pools over oceans and their interactions with the larger-scale environment. *Surv Geophys*, 38:1283–1305, 2017. 2, 7